JOURNAL OF GEOPHYSICAL RESEARCH, VOL. 99, NO. B11, PAGES 21,835–21,855, NOVEMBER 10, 1994

The 1989 Loma Prieta earthquake imaged from inversion of geodetic data

Thóra Árnadóttir [1] and Paul Segall
Department of Geophysics, Stanford University, Stanford, California

Abstract. We invert geodetic measurements of coseismic deformation from the 1989 M_S7.1 Loma Prieta earthquake to determine the geometry of the fault and the distribution of slip on the fault plane. The data include electronic distance measurements, Global Positioning System and very long baseline interferometry vectors, and elevation changes derived from spirit leveling. The fault is modeled as a rectangular dislocation surface in a homogeneous, elastic half-space. First, we assume that the slip on the fault is uniform and estimate the position, orientation, and size of the fault plane using a nonlinear, quasi-Newton algorithm. The best fitting dislocation strikes N48°± 4°W and dips 76°± 9°SW, consistent with the trend of the aftershock zone and moment tensor solutions. Bootstrap resampling of the data is used to graphically illustrate the uncertainty in the location of the rupture plane. The 95% confidence envelope overlaps the aftershock zone, arguing that there is not a significant discrepancy between the geodetic data and the aftershock locations. Second, we estimate the slip distribution using the best fitting uniform slip fault orientation but increase the fault length to 40 km and the downdip width to 18 km. The fault is divided into 162 subfaults, 18 along strike and 9 along dip. Each subfault is allowed to have constant right-lateral and reverse components of slip. We then solve for the slip on each subfault that minimizes a linear combination of the norm of the weighted data residual and the roughness of the slip distribution. The smoothing parameter, which determines the relative weight put on fitting the data versus smoothing the slip distribution, is chosen by cross validation. Simulations indicate that cross-validation estimates of the smoothing parameter are nearly optimal. The preferred slip distribution is very heterogeneous, with maximum strike slip and dip slip of about 5 and 8 m, respectively, located roughly 10 km north of the hypocenter. There is insignificant dip slip in the southeastern most part of the fault, causing the rake to vary from nearly pure right-lateral in the southeast to oblique right-reverse in the northwest. The change in rake is consistent with a uniform stress field if the fault dip increases by about 10° toward the southeast, as indicated by the aftershock locations. There was little slip above 4 km depth, consistent with the observation that there was little, if any, surface rupture.

Introduction

The M_S7.1, 1989 Loma Prieta earthquake was located within a dense network of seismic and geodetic stations, and the event was large enough to be well recorded by global seismic stations. This provided an unusual opportunity to study the earthquake source mechanism by inversion of local geodetic data, as well as teleseismic and local seismic data, including strong motion acceleration data. Numerous studies of the Loma Prieta earthquake have been published in the July, August, and September 1990 issues of *Geophysical Research Letters* [*McNally and Ward*, 1990] and the October 1991 special issue of the *Bulletin of the Seismological Society of America* [*Hanks and Krawinkler*, 1991].

Despite extensive research, a number of important questions about the earthquake remain. Early inversions of geodetic data had found the best fitting uniform slip dislocation surface to be located a few kilometers west of the zone of aftershocks [*Lisowski et al.*, 1990; *Marshall et al.*, 1991]. In particular, *Marshall et al.* [1991] found from modeling the coseismic elevation changes that the rupture surface was offset ~ 3 km southwest of the aftershocks. Given the heterogeneity of the mechanisms, they suggested that the rupture surface might be distinct from the aftershock zone.

[1] Now at Department of Geology, Victoria University, Wellington, New Zealand.

Paper number 94JB01256.
0148-0227/94/94JB-01256$05.00

Eberhart-Phillips and Stuart [1992] suggested that this discrepancy was due to contrast in elastic properties across the fault. *Árnadóttir et al.* [1992] showed that in the case of the leveling data, the major part of the discrepancy disappeared if one accounted for correlations, which are inherent in leveling data, in the estimation procedure. In the case of the *Lisowski et al.* [1990] data, *Árnadóttir et al.* [1992] found that part of the discrepancy was accounted for by failure of the trial and error methods used to find the best fitting dislocation geometry. In a reexamination of the leveling data, *Marshall and Stein* [1994] use a two-dimensional boundary element method to approximate the effect of elastic heterogeneity in three dimensions. They find that accounting for a compliant wedge in the hanging wall of the fault, as suggested by *Eberhart-Phillips and Stuart* [1992], and the correlations in the leveling data, as suggested by *Árnadóttir et al.* [1992], that the discrepancy is insignificant. Even so, there is a clear tendency for the estimated dislocation surfaces to be offset toward the southwestern edge of the aftershock zone. The problem has not been fully resolved for a number of reasons: (1) None of the previous studies simultaneously inverted all of the available geodetic data; (2) many studies used trial and error estimation methods and did not compute rigorous uncertainties in the fault location; and (3) previous studies have not used Green's functions appropriate for a laterally varying three-dimensional half-space.

In this study we make use of all the high-quality geodetic data obtained before and after the earthquake. By combining all the geodetic data sets, we get better information about the three-dimensional deformation field, thus obtaining better constraints on the geometry of the fault that ruptured and the amount of slip. Furthermore, we have developed a method to invert geodetic data to obtain the best uniform slip dislocation geometry using a nonlinear estimation method. We also introduce the use of a bootstrap method for determining confidence limits in the geometric parameters. Results here are limited to uniform elastic half-spaces; however, *Du et al.* [1994] show how first-order perturbation methods can be used to approximate Green's functions in three-dimensional media with laterally varying elastic properties.

A second unresolved problem has been to determine how the slip is distributed on the fault plane. Several inversions of the strong motion data have been conducted for spatially varying fault slip [*Beroza*, 1991; *Hartzell et al.*, 1991; *Steidl et al.*, 1991; *Wald et al.*, 1991; *Horton et al.*, 1994; *Steidl and Archuleta*, 1994]. Determination of the static slip distribution from strong motion data is complicated by the fact that the data depend on slip amplitude, rupture time, and rise time. Geodetic data, on the other hand, are independent of rupture dynamics. The models derived from the strong motion data (some of which also use geodetic data) have many features in common. Most models find two areas of concentrated slip in the northwest and southeast parts of the fault, with surprisingly little slip updip from the hypocenter. To date, there have not been inversions of the full geodetic data set to compare these results to. In this study we conduct inversions of the geodetic data to determine the spatial distribution of fault slip.

A surprising result of the slip models presented by *Beroza* [1991] and *Steidl et al.* [1991] is the large variation of rake as a function of position on the fault. The rake changes from nearly pure thrust in the northwest part of the rupture to almost purely right-lateral strike slip in the southeastern part. On the other hand, the model by *Wald et al.* [1991] has a similar, oblique rake in both areas. The results of *Hartzell et al.* [1991] show intermediate variations. Analysis of the leveling data by *Marshall et al.* [1991] also suggests more dip slip to the northwest and more strike slip to the southeast. We explore this question further by inverting the geodetic observations and suggest possible mechanisms for the variation in slip direction.

Geodetic Data

The data used in this study are summarized in Figure 1. We analyze electro-optical distance measurements (EDM) and Global Positioning System (GPS) measurements collected by *Lisowski et al.* [1990], very long baseline interferometry (VLBI) data reported on by *Clark et al.* [1990], and GPS data reported on by *Williams et al.* [1993]. The GPS and VLBI data give changes in the three-dimensional relative position vectors between stations. The EDM measurements give only the change in the baseline length between stations.

The EDM and GPS data collected by *Lisowski et al.* [1990] were corrected for interseismic deformation as well as for coseismic deformation caused by the 1979 Coyote Lake, 1984 Morgan Hill, and the 1986 Mount Lewis earthquakes. The GPS data collected by *Williams et al.* [1993] in the Santa Cruz-Watsonville area span a very short interval and require no interseismic correction. The VLBI measurements at Fort Ord were made at the station Fort Ord S, whereas the GPS measurements were made a few hundred meters away at Brush 2. Since both are several source depths away from the epicenter one can assume that these two stations moved by the same amount in the earthquake. This allows us to determine the displacements of the entire network relative to VLBI stations on stable North America (Figure 2a). The largest horizontal displacement is 41 cm at station Traill.

We also analyze the spirit leveling data reported on by *Marshall et al.* [1991]. Leveling networks in the Loma Prieta area were resurveyed by the National Geodetic Survey (NGS) and the U.S. Geological Survey (USGS) from February through June 1990 (Figure 1). The preearthquake surveys were performed by NGS and USGS between 1948 and 1989. Lines 4, 5, 6, and 7, which span the interior of the network, were measured in 1948-1953. These are the least precise measurements (third-order, single-run leveling), and several bench marks were destroyed between the preearthquake and postearthquake surveys. The leveling data were corrected for subsidence induced by groundwater withdrawal by *Marshall et al.* [1991]. The largest corrections are 10-20 mm, in San Jose (lines 1 and 3) and

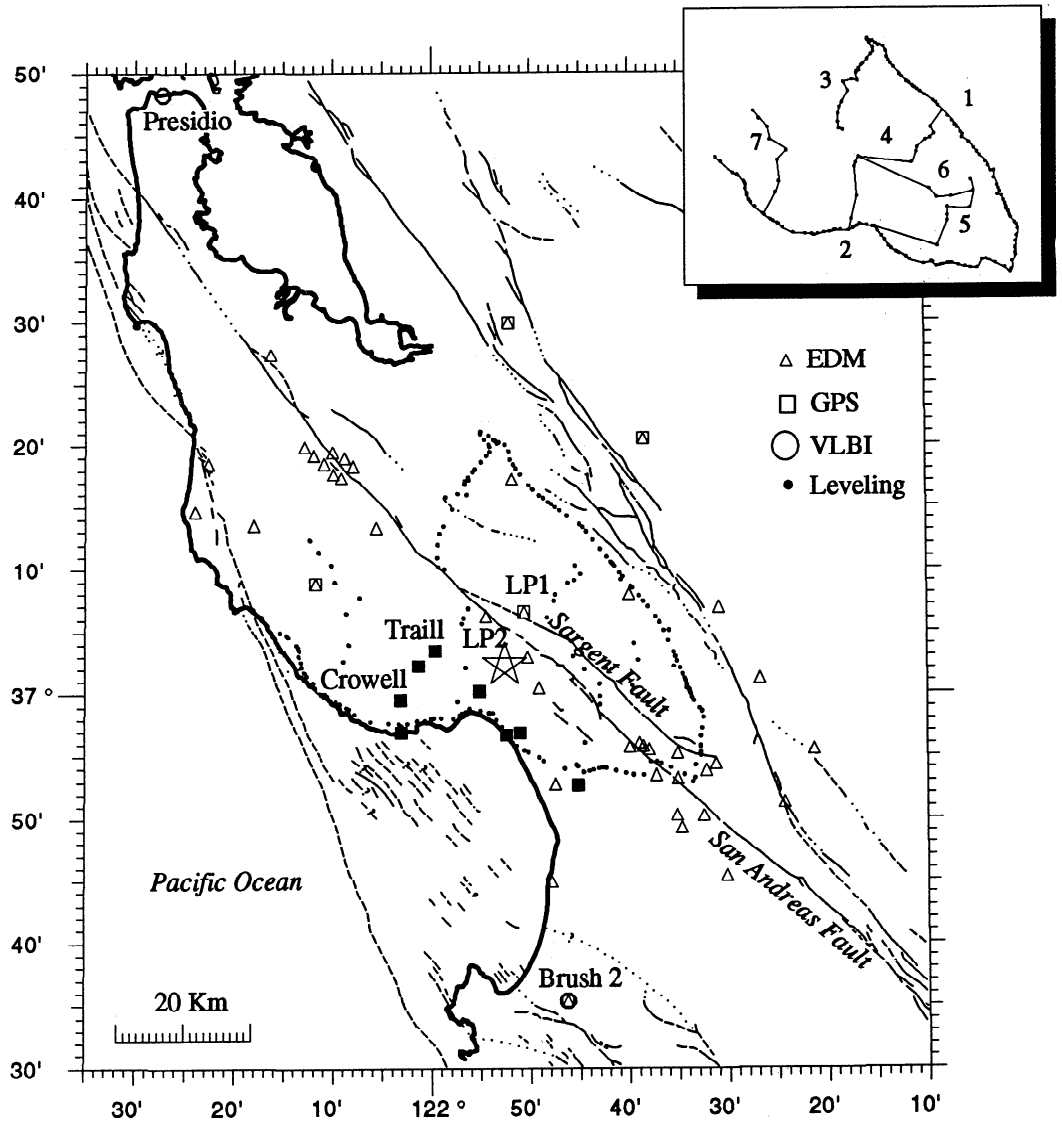

Figure 1. A map of the San Francisco Bay Area in California showing major faults and coastline (bold) and the network of geodetic stations used in this study. A few stations referred to in the text are labeled. The triangles are EDM stations, the squares are GPS stations, the circles are VLBI stations, and the dots are leveling bench marks. The GPS stations from *Williams et al.* [1993] are shown with solid squares. The insert shows the leveling line numbers referred to in the text. The main shock epicenter location is indicated with a star.

near Watsonville (line 2). They also applied small corrections for the coseismic deformation due to the 1979 Coyote Lake and 1984 Morgan Hill earthquakes (line 1). The coseismic vertical displacements calculated from the observed section height differences are shown in Figure 3a. The largest signal is 59 cm of uplift in the central part of the network.

Inversion for Fault Geometry

Method

We start by determining the fault geometry that best describes the observed surface deformation. The fault is represented by a rectangular dislocation, with uniform slip, embedded in a homogeneous, isotropic, elastic half-space [e.g., *Okada*, 1985]. Figure 4 shows the dislocation model and the nine parameters that we estimate: fault length L, width W, depth z_0, dip δ, strike ϕ, location (x_0, y_0), strike slip SS, and dip slip DS. The slip on the dislocation is initially assumed to be constant. In a later section this assumption is relaxed, and we estimate the spatial distribution of slip. We seek a set of the nine fault parameters that minimize the weighted residual sum of squares (RSS), $\mathbf{r}^T\Sigma^{-1}\mathbf{r}$. Here $\mathbf{r}$ is the residual vector, the difference between the observed and predicted data, and Σ is the data covariance matrix. This problem is nonlinear since the predicted surface displacements are nonlinear functions of the fault geometry. We use a nonlinear optimization algorithm, NPSOL [*Gill et al.*, 1986], to find the set of fault parameters $\hat{\xi}$ that minimizes $\Phi(\xi)$, where $\Phi(\xi) = \mathbf{r}^T\Sigma^{-1}\mathbf{r}$.

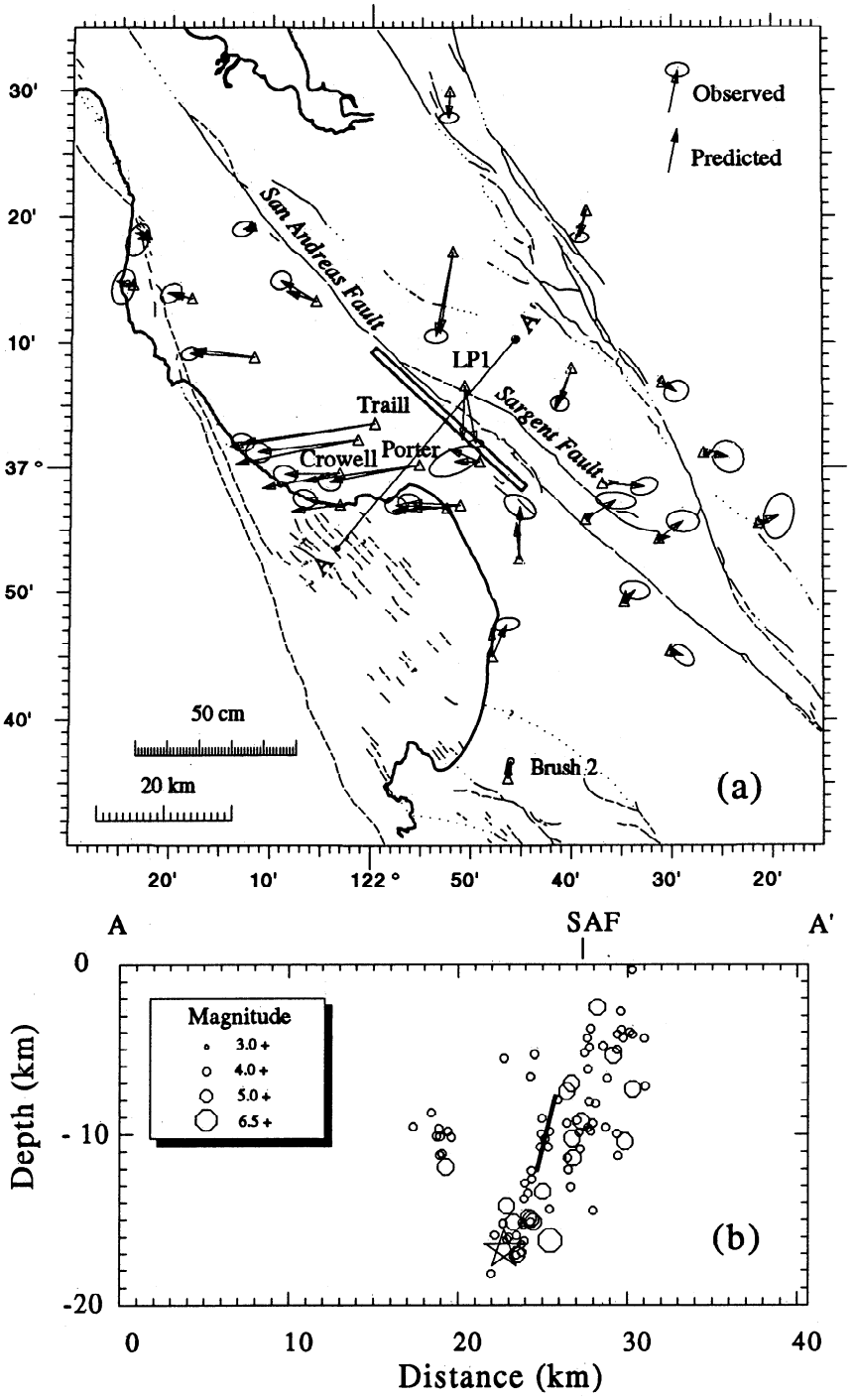

Figure 2. (a) Observed and predicted horizontal displacements from the best uniform slip dislocation model. The surface projection of the fault model is shown by a rectangle. A few stations referred to in the text are labeled. (b) Location of the dislocation in cross section AA′. The locations of aftershocks with $M \geq 3.0$ recorded from October 18 to October 31, 1989, are shown with hexagons and the main shock epicenter is indicated by a star.

In this study, we employ the quasi-Newton method [*Gill et al.*, 1981] which is effective when the first and second derivatives of the function $\Phi(\xi)$ are not simply computed analytically. Quasi-Newton methods require only that $\Phi(\xi)$ be at least twice continuously differentiable. In the quasi-Newton method, as in Newton's method, a quadratic model of the objective function $\Phi(\xi)$ is constructed by taking the first three terms of the Taylor series expansion about a point ξ_k:

$$\Phi_{k+1} \approx \Phi_k + \nabla\Phi_k^T \delta\xi_k + \frac{1}{2}\delta\xi_k^T H_k \delta\xi_k \,, \qquad (1)$$

where $\Phi_k = \Phi(\xi_k)$, $\nabla\Phi_k = \nabla\Phi(\xi_k)$ is the gradient of Φ, $H_k = H(\xi_k)$ is the second derivative matrix of Φ (also

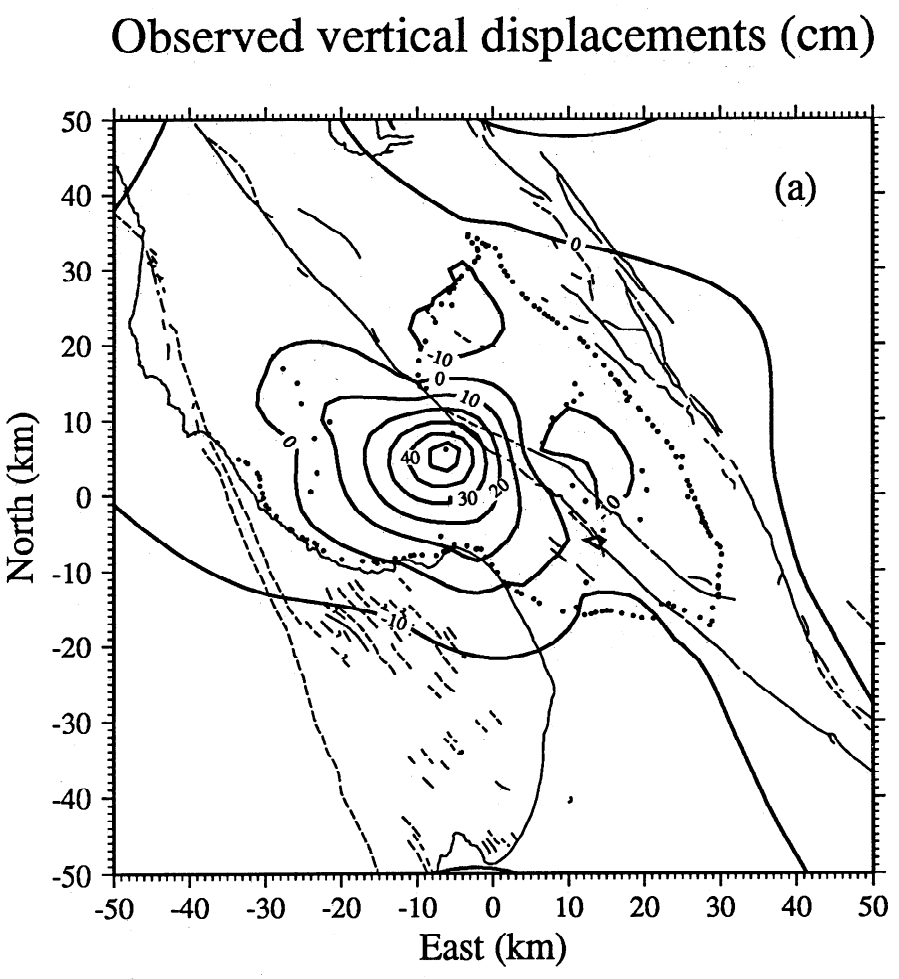

Figure 3. (a) Interpolated contours of vertical displacements in centimeters, calculated from observed section height differences. The locations of the bench marks are shown with dots.

called the Hessian), and $\delta\xi_k = \xi_{k+1} - \xi_k$. Since Φ is a stationary point at the minimum of equation (1),

$$\frac{\partial \Phi_{k+1}}{\partial \delta \xi_k} = 0 . \tag{2}$$

Hence the quadratic function is minimized as a function of $\delta\xi_k$ by solving Newton's equation

$$H_k \delta\xi_k = -\nabla\Phi_k . \tag{3}$$

The solution is the Newton search direction. NPSOL solves equation (3) by Cholesky decomposition and backsubstitution.

The quasi-Newton method is based on the fact that an approximation to the curvature of a nonlinear function along a line can be computed from two values of the gradient on the line without explicitly forming the Hessian matrix. The curvature of Φ along $\delta\xi$ is given by $\delta\xi^T H_k \delta\xi$, which can be approximated using only first-order information:

$$\delta\xi^T H_k \delta\xi \approx (\nabla\Phi_{k+1} - \nabla\Phi_k)^T \delta\xi . \tag{4}$$

We compute $\nabla\Phi(\xi)$ numerically using a finite difference approximation.

The algorithm works in the following manner: The values of $\Phi(\xi_0)$ and $\nabla\Phi(\xi_0)$ are calculated for a given starting value ξ_0. The next value, ξ_1, is calculated from $\xi_1 = \xi_0 + \delta\xi$, where $\delta\xi$ is a solution to equation (3), given $\nabla\Phi(\xi_0)$ and $H(\xi_0)$. The initial value of the Hessian is assumed to be the identity matrix, $H(\xi_0) = I$. After ξ_1 has been computed, a new Hessian approximation $H(\xi_1)$ is estimated by $H(\xi_1) = H(\xi_0) + U_0$, where U_0 is an updating matrix, which takes into account the new cuvature information. The updated Hessian must be symmetric and positive definite. Then the next step is calculated. This sequence is repeated until the solution converges to a minimum, that is, until we find $\hat{\xi}$ such that $\Phi(\hat{\xi}) < \Phi(\xi)$ for all $\hat{\xi} \neq \xi$.

NPSOL allows one to specify upper and lower bounds, as well as linear and nonlinear constraints on the variables. For an unconstrained problem the following conditions are necessary at the minimum: (1) The gradient at the minimum is zero ($\nabla\Phi(\hat{\xi}) = 0$) and (2) $H(\hat{\xi})$ is positive definite, that is, $\mathbf{s}^T H(\hat{\xi})\mathbf{s} > 0$ for all nonzero vectors $\mathbf{s}$. In the case of a constrained problem, conditions 1 and 2 hold for all parameters not subject to a constraint. If a parameter is at a bound, the condition for a minimum is that the gradient is directed

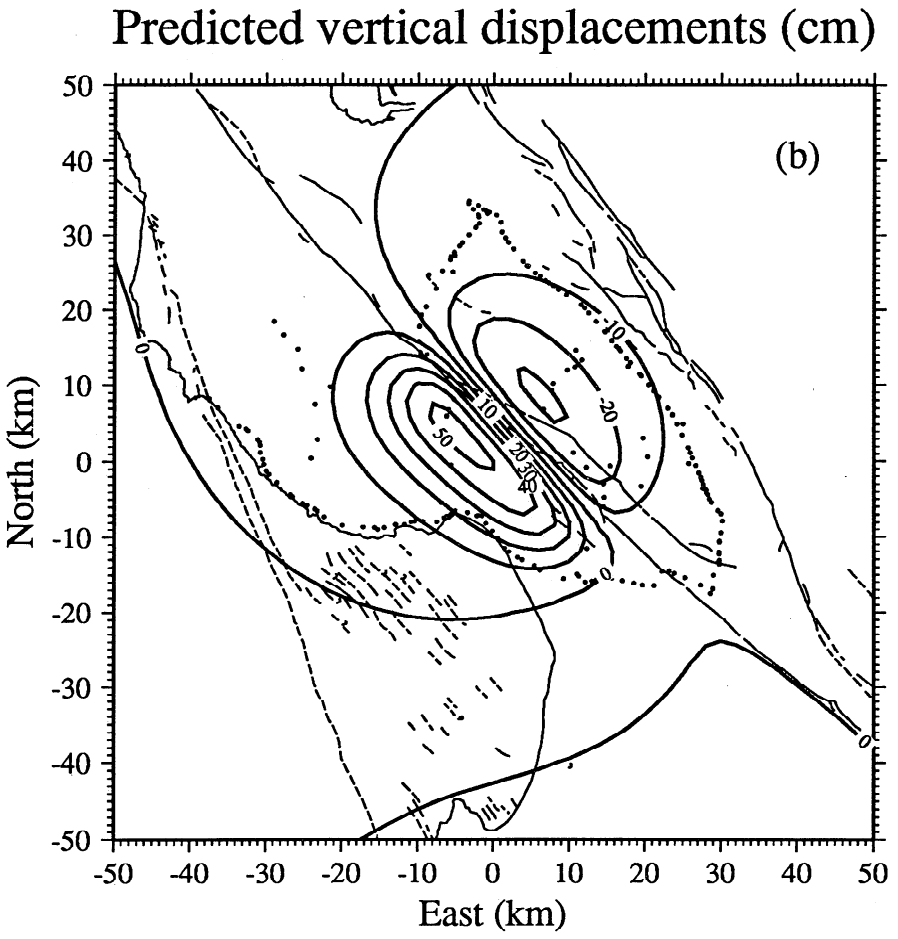

Figure 3. (b) Predicted vertical displacements from the best uniform slip model (in centimeters).

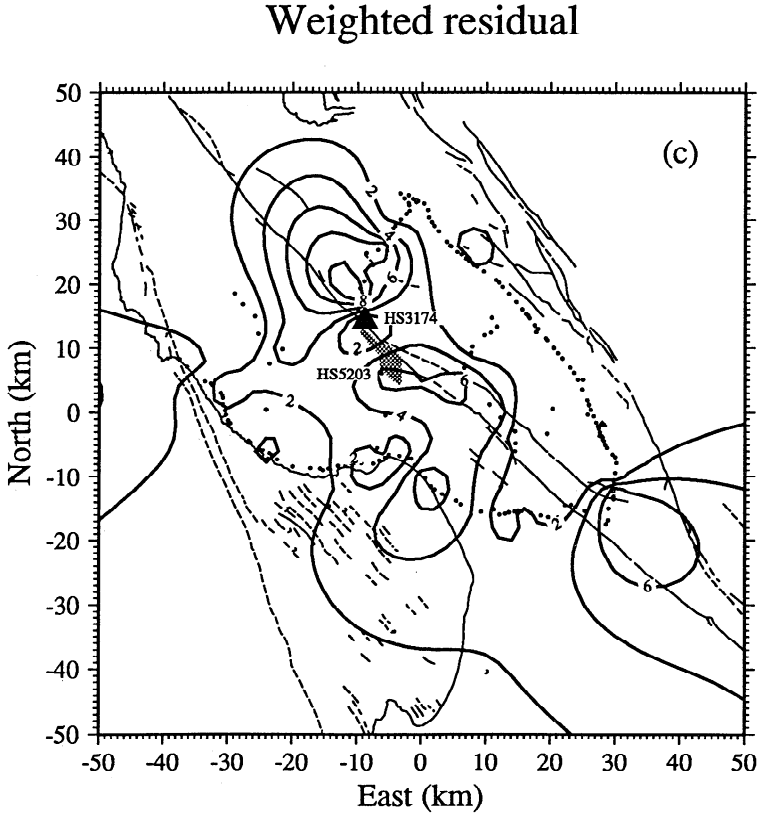

Figure 3. (c) Weighted residual of the vertical displacements and the best uniform slip model for the combined data. The weighted residual has units of σ standard deviation. The solid triangle shows the location of station HS3174 that has the largest residual, 20σ. The shaded region shows the area of extensive ground cracks [from *U.S. Geological Survey Staff*, 1989].

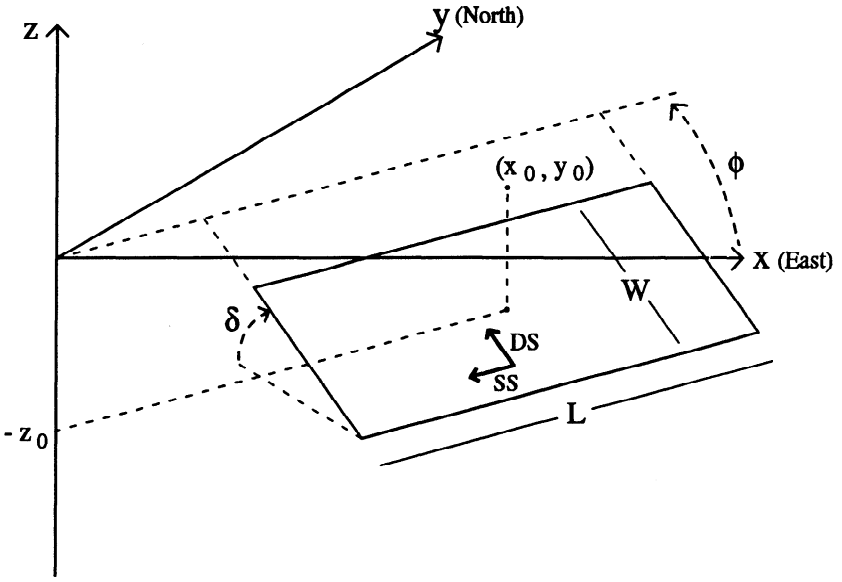

Figure 4. Dislocation model parameters: length along strike L, width along dip W, depth to center z_0, dip δ, strike ϕ, location of center (x_0, y_0), right-lateral strike slip SS, and reverse dip slip DS.

away from the bound, i.e., that the gradient is positive at a lower bound and negative at an upper bound. We place very broad upper and lower bounds on the fault parameters and add a constraint that the upper edge of the dislocation does not extend above Earth's surface.

Confidence Intervals for Fault Parameters

To assess how well the model is constrained by the data, it is important to estimate confidence intervals for the model parameters. This is not a straightforward procedure when the model is a nonlinear function of the data. In this section we discuss two methods to estimate 95% confidence intervals for the fault parameters.

Approximate bounds are found by linearizing the model around the minimum $\hat{\xi}$. An ellipsoidal confidence region for the parameters can by found from

$$\Phi(\hat{\xi_\alpha}) = \Phi(\hat{\xi})[1 + \frac{m}{n-m} F(m, n-m, 1-\alpha)] \quad (5)$$

[*Draper and Smith*, 1981]. As before, $\Phi(\hat{\xi})$ is the weighted residual sum of squares (RSS) for the set of optimal fault parameters $\hat{\xi}$. $F(m, n-m, 1-\alpha)$ is the F distribution with m and $n-m$ degrees of freedom at a $100 \times (1-\alpha)\%$ confidence level, where m is the number of model parameters (here m=9) and n is the number of data (here n=333). $\Phi(\hat{\xi_\alpha})$ is the "cutoff" value of the RSS for a given confidence level, and $\hat{\xi_\alpha}$ are the upper and lower bounds on the parameters $\hat{\xi}$ for that confidence level. We find the confidence intervals for the fault parameters allowing one parameter to vary while the other parameters are fixed at their optimal values. The advantage of the F test is that it is simple and not computationally intensive. The drawbacks are that the F test assumes that the data errors are normally distributed and the confidence intervals are only approximate, since Φ is nonlinear.

We also construct confidence intervals using the bootstrap method [e.g., *Efron and Tibshirani*, 1986]. We draw a resample $d_1^*, \cdots, d_n^*$ at random from the original data $d_1, \cdots, d_n$ with replacement, that is, allowing individual data points to be sampled more (or less) than once. We then estimate the model parameters $\hat{\xi}^*$ from the resampled data using the quasi-Newton algorithm. The resampling and estimation steps are repeated B times yielding B independent estimates of the model parameters. The parameter estimates are then ordered such that $\hat{\xi}^*_{[1]} \leq \cdots \leq \hat{\xi}^*_{[B]}$. The two-sided $100 \times (1-\alpha)\%$ bootstrap percentile method interval for ξ is $[\hat{\xi}^*_{([\frac{\alpha}{2}B]+1)}, \hat{\xi}^*_{([(1-\frac{\alpha}{2})B]+1)}]$, where $[\frac{\alpha}{2}B]$ denotes the integer part of $\frac{\alpha}{2}B$. For example, if $B = 2000$, then the 95% confidence lower bound is $\hat{\xi}^*_{[51]}$, while the upper bound is $\hat{\xi}^*_{[1951]}$. The bootstrap percentile method is based on the premise that the distribution of $\hat{\xi}^*$, the bootstraped version of $\hat{\xi}$, is similar to the unknown distribution of $\hat{\xi}$.

The advantage of the bootstrap method is that it does not make assumptions about the distribution of errors in the data. Rather, the true distribution is built up from the data by resampling. The disadvantages of the bootstrap method is that it is computationally intensive, and the confidence intervals are only approximate. Better estimates of the confidence intervals can be constructed using a double-bootstrap method [e.g., *Hall and Martin*, 1988], but that requires B^2 rather than B resamples.

Results

We determine the optimal uniform slip dislocation geometry using the methods described above (see Table 1). The fault is found to be about 30 km long along strike. It extends vertically from about 8 km to 12

km depth, dips 76°southwest, and strikes N48°W, with 5.2 m of strike-slip and 4.6 m of dip-slip motion. The geodetic moment is $M_0 = 2.9 \times 10^{19}$ N m, assuming a shear modululs of 3.0×10^{10} Pa, and the rake is 139°. This model is in good agreement with the major double-couple orientation (strike of N52°± 3°W, dip of 67 ± 5° and rake of 133°± 8°) and seismic moment (2.4 - 3.2 $\times 10^{19}$ N m) estimated from seismic data [*Wallace et al.*, 1991]. We use 333 data (n) to estimate nine fault parameters (m), so the solution has 324 degrees of freedom. The mean square error ($\mathrm{MSE} = \frac{1}{n-m}\,\mathbf{r}^T\Sigma^{-1}\mathbf{r}$) is 12 and the misfit of the model is equal to $\sqrt{\mathrm{MSE}} = 3.5$. The misfit for the leveling data alone ($n = 209$) and the combination of EDM, GPS, and VLBI data ($n = 124$) is 3.5 for both sets of data, implying that the data sets are weighted equally in the inversion and that neither data set is fit very well. This is in part due to the uniform slip assumption which is relaxed below.

Figure 2a compares the predicted horizontal displacements for the uniform slip model with the observed displacements. The simple model predicts the data fairly well; the largest differences are 8.3 cm at Crowell and 8.0 cm at Porter. Figure 2b shows the location of the model in the cross section AA′, relative to the location of aftershocks with $M \geq 3.0$ recorded from October 18 to October 31, 1989. The imaged dislocation surface is well within the zone of aftershocks. The lower edge of the dislocation does not reach the depth of the hypocenter. However, we observe a trade-off between the fault width and the magnitude of the slip on the fault. A wider fault with less slip produces a similar pattern of surface displacements with only slightly higher residual. This has also been observed in other studies [*Árnadóttir et al.*, 1992; *Marshall et al.*, 1991; *Snay et al.*, 1991].

Figures 3a and 3b show the observed and predicted vertical displacements respectively. Figure 3c shows the weighted leveling residuals, which are the section height differences divided by the standard deviation of the data and the square root of the section lengths [see *Árnadóttir et al.*, 1992]. The largest residuals are in the area northwest of Loma Prieta peak, up to 20σ at bench mark HS3174 (shown with solid triangle in Figure 3c). The residuals for the rest of the network are for the most part below 5σ.

Further examination of the residuals indicates three outliers, leveling bench marks HS3174 and HS5203 and the EDM baseline LP1-LP2 [*Árnadóttir*, 1993]. Large shaking-induced gravitational spreading of ridges and downslope movement was observed along Summit Road and Skyland Ridge in the Santa Cruz Mountains [e.g., *Ponti and Wells*, 1991]. The shaded area in Figure 3c shows the approximate location of this zone of inelastic deformation. The stations with the largest residuals are located in, or close to, this area. The large residuals could therefore be due to inelastic deformation caused by ground ruptures and land sliding, which would not be predicted by the elastic model. Removing data from these three stations decreases the misfit to 3.0 but does not change the model substantially. The distribution of residuals is not Gaussian; however, model estimates based on minimization of the L_1 norm are not significantly different from the least squares solutions presented here [*Árnadóttir*, 1993].

Figure 5 shows the misfit as a function of individual fault parameters, where one parameter is allowed to vary and the other parameters are fixed at their optimal values. Models with misfit less than 3.7 are within the 95% confidence limit (equation (5)). Figure 5 does not show the correlation between the various fault parameters, for example the trade-off between the fault width and the amount of slip on the fault.

We also use the bootstrap method to estimate 95% confidence intervals. The results of 2000 models from bootstrap resamples of the data are shown in Table 1. Comparing the first and second row of Table 1, we see that the mean of the bootstrap estimates are in good agreement with the optimal model determined using all the data; the largest difference is in the fault length (3 km), but the value is still within the uncertainty estimated by both methods. The uncertainties in the model parameters estimated by the bootstrap percentile method tend to be larger than those determined by the F test. In particular, the large range in the fault width and amount of slip obtained from the bootstrap models reflects the trade-off between these parameters.

To illustrate graphically the results of the bootstrap calculations, Figure 6 shows a cross section of the "density" of bootstrap estimated fault models that are within the 95% confidence level. Figure 6 was constructed by girding the area in the cross section. The density in each element was calculated by summing the normalized distance all the bootstrapped dislocation surfaces traversed each element. The density is shown with a gray shade, where the darker shade implies a larger number of estimated fault models pass through that region. The solid line is the mean of the bootstrap models and the dashed line is the optimal model obtained using all the data. The extent of the shaded region in Figure 6 demonstrates the variability in the possible fault models that fit the geodetic data reasonably well. The area just southwest of the mean bootstrap model (solid line) has a higher density of fault models and narrower aperture than the area to the northeast. The shaded region widens with depth, as we would expect, since the location of the upper edge of the fault is better constrained than the lower edge. From this we conclude that the data can be fit with faults located in the aftershock zone, although there is still a slight bias toward the southwest edge of the aftershock zone.

The uncertainty in the fault location is in part due to the paucity of stations near the fault. Data from Loma Prieta peak and surrounding area are important in determining the location of the fault as well as the fault dip and width. None of the models derived from geodetic or seismic data produce good fit to these data. *Lisowski et al.* [1994] note that there was considerable relative coseismic motion between the stations on Loma Prieta peak. There were no ground cracks observed, but strong shaking in the earthquake may have caused monument instability in the area.

We have experimented with more complicated fault geometries, including adding a shallow vertical fault

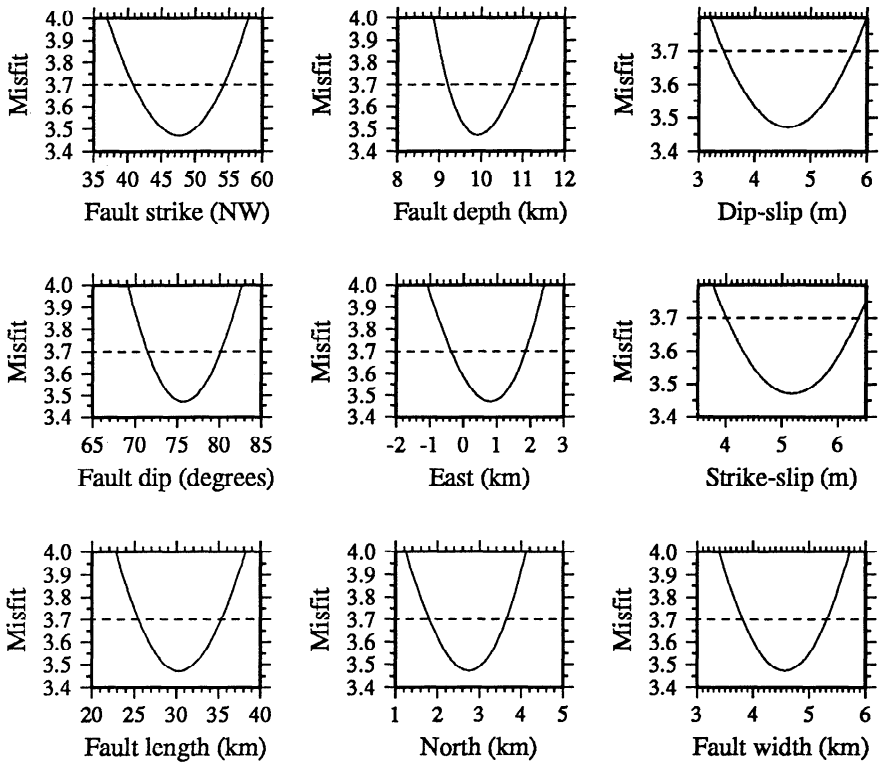

Figure 5. Misfit as a function of fault parameters for the uniform slip model that best fits the Loma Prieta geodetic data used in this study. Each parameter is varied while keeping the other parameters fixed at their optimal values. The dashed line is the "cutoff" value for the misfit from the F test. The 95% confidence level is the range of values of the parameters that have misfits less than 3.7.

segment, similar to the "kinked" model of *Snay et al.* [1991]. The shallow vertical fault segment is poorly constrained by the data. With this geometry, we did not find any models that significantly improved the fit to the data and were at the same time consistent with the aftershock locations. We also allowed two independent faults; one fault located northwest of the epicenter and the other to the southeast. The best-fit model, in this case, provided a slightly better fit (misfit of 3.4) to the data than the single fault model. The geometry is similar to the single fault uniform slip model, except for the rake and slip. The rake on the northwest fault is 134°, with about 8 m of slip, while the rake on the southeast fault is 161°, with about 2 m of slip. This is an indication that the geodetic data are better fit by a heterogeneous slip distribution, which is addressed in a later section.

We also attempted to see if the geodetic data are capable of resolving dilatancy during the earthquake by allowing for relative motion normal to the fault plane. This yielded a slight fault compaction equivalent to 3% of the slip, however the compaction is not significant. *Savage et al.* [1994] suggest that 10 cm of fault compaction occurred following the Loma Prieta earthquake, suggesting that comparable amounts of dilatancy accompanied the earthquake. Constraining the fault dilation to 10 cm increases the misfit to the data; however, the model is still acceptable at the 95% confidence level. We conclude that the geodetic data do not place useful constraints on the amount of dilatancy for this event.

Simulations

Inversions of strong motion data demonstrate that the slip was spatially heterogeneous [*Beroza*, 1991; *Steidl et al.*, 1991; *Wald et al.*, 1991]. To investigate how the assumption of uniform slip affects the estimated fault geometry when the slip is in fact nonuniform, we generated synthetic data (EDM, GPS, VLBI, and leveling) from a forward model with spatially varying slip. Noise was added to the calculated data such that the signal to noise ratio $(\frac{1}{n}\mathbf{d}^T\Sigma^{-1}\mathbf{d})^{1/2}$ is comparable to that in the Loma Prieta geodetic data set.

The synthetic model fault extends from 2 to 20 km depth along dip, 40 km along strike, dips 76°SW, and has a strike of N48°W. Figure 7 shows the slip distribution on the fault. There are two slip maxima in this model, one in the northwest part of the fault and the other in the southeast part of the fault. The model has the same magnitude of strike slip and dip slip, so the rake is everywhere 135°. The fault parameters of the synthetic model are given in Table 1. To compare this model with uniform slip models, we use the centroid depth as the depth to the fault center and take the average of the strike-slip and dip-slip magnitudes on the fault.

The synthetic data are then inverted to obtain the optimal fault geometry. We found a consistent set of fault parameters (see Table 1) for a range of starting models. We see from Table 1 that all the fault parameters are well resolved. The estimated average rake is 134°, while

the actual rake is 135°. The estimated moment is 4% greater than the actual moment, and the predicted fault dip is 2° greater than in the actual model. The confidence intervals calculated from the bootstrap (Table 1) include the correct value for all of the parameters.

The misfit, the square root of the normalized weighted residual sum of squares, to the model determined by the quasi-Newton optimization is 1.11. According to equation (5), models with misfits in less than 1.14 are within the 95% confidence level. Interestingly, the misfit for the correct fault geometry with uniform slip is 2.04, which is well outside the 95% confidence level. This suggests that the large misfit to the uniform slip model that we observe in the Loma Prieta data is in large part due to spatial variations in slip.

Figure 8 shows the location of the estimated and actual fault models in map and cross section. They are virtually identical. Most of the slip in the example is below 6 km depth which biases the estimated uniform slip model to greater depth. The centroid depth of the uniform slip estimate is close to the correct centroid depth of the distributed-slip model. In summary, the results from these simulations indicate that the estimated geometry assuming uniform slip is likely to be very close to the actual fault geometry, even if the slip is heterogeneous. In the next section we use the estimated fault geometry and invert for the slip distribution.

Inversion for Distributed Slip

Method

Our starting point is the fault geometry found in the previous section. We increase the fault length along strike from 30 km to 40 km, and the downdip width from 5 km to 18 km, to allow the slip to taper to zero at the fault edges. The fault has a dip of 76°SW and strikes N48°W. We adopt a discrete basis and divide the fault into a grid of 162 subfaults, with uniform slip in both the strike-slip and dip-slip components. Each subfault extends 2.22 km horizontally and 2.0 km vertically.

The geodetically determined surface deformation (the data **d**) is a linear function of the slip distribution on the fault **s** of the form

$$\mathbf{d} = G\mathbf{s} + \boldsymbol{\epsilon}\,, \tag{6}$$

where G is a matrix of Green's functions and $\boldsymbol{\epsilon}$ is the measurement error. The Green's functions are calculated for a homogeneous, elastic half-space [e.g., *Okada*, 1985]. We assume that the errors are normally distributed with mean zero and covariance matrix Σ, $\boldsymbol{\epsilon} \sim N(0, \Sigma)$. We transform the problem to $\mathbf{d}' = G'\mathbf{s} + \boldsymbol{\epsilon}'$, where $\boldsymbol{\epsilon}' \sim N(0, \mathrm{I})$ and I is the identity matrix. Here, $\mathbf{d}' = T\,\mathbf{d}$ and $G' = T\,G$, where T is the weight matrix given by the inverse of the Cholesky factorization of the data covariance matrix, $\Sigma^{-1} = T^T T$. We drop the primes from the notation in the remainder of the discussion. To approximate a continuous slip distribution, the model subfaults are made reasonably

Table 1. Fault Parameters for Uniform Slip Models

Model	Length[a], km	Depth[b], km	Width[c], km	Dip, °SW	Strike	Location[d], km East	Location[d], km North	Strike Slip, m	Dip Slip, m	Moment, $\times 10^{19}$ N m
Loma Prieta Geodetic Data										
F test[e]	30.3 ± 5.0	9.9 ± 1.0	4.6 ± 1.0	$75.8° \pm 4.0$	N47.6°W ± 7.0	0.8 ± 1.0	2.8 ± 1.0	5.2 ± 1.1	4.6 ± 1.1	2.9
Bootstrap[f]	$32.6^{+3.9}_{-4.6}$	$9.3^{+1.2}_{-0.8}$	$4.3^{+6.7}_{-2.9}$	$74.7°^{+9.3}_{-9.1}$	N49.3°W $^{+3.7}_{-4.2}$	$-0.1^{+2.8}_{-2.3}$	$3.6^{+1.4}_{-1.3}$	$6.4^{+8.4}_{-4.7}$	$5.8^{+7.5}_{-3.9}$	2.7
Synthetic Data										
Actual model[g]	40.0	12.6[h]	18.0	75.8°	N47.6°W	0.7	2.6	0.83[i]	0.83[i]	2.5
F test[e]	39.8 ± 1.2	13.0 ± 0.4	17.8 ± 0.3	$77.4° \pm 0.5$	N47.5°W ± 0.6	0.5 ± 0.2	2.3 ± 0.2	0.87 ± 0.03	0.89 ± 0.03	2.6
Bootstrap[f]	$39.5^{+1.0}_{-1.7}$	$12.9^{+0.7}_{-2.3}$	$17.3^{+2.3}_{-15.6}$	$77.4°^{+5.8}_{-1.5}$	N47.4°W $^{+0.6}_{-2.4}$	$0.4^{+1.2}_{-0.4}$	$2.3^{+0.4}_{-0.4}$	$1.3^{+8.0}_{-0.5}$	$1.2^{+6.0}_{-0.4}$	2.6

[a] Length along strike.
[b] Depth to the center of the fault.
[c] Width of the fault along dip.
[d] Location of the center of the fault relative to the main shock hypocenter.
[e] Best model from all the data, 95% confidence level estimated from F test.
[f] Mean of 2000 bootstrap models from resamples of the data, 95% confidence level estimated from percentile method interval.
[g] Distributed-slip model shown in Figure 7.
[h] Centroid depth for the distributed-slip model.
[i] Average slip for the distributed-slip model.

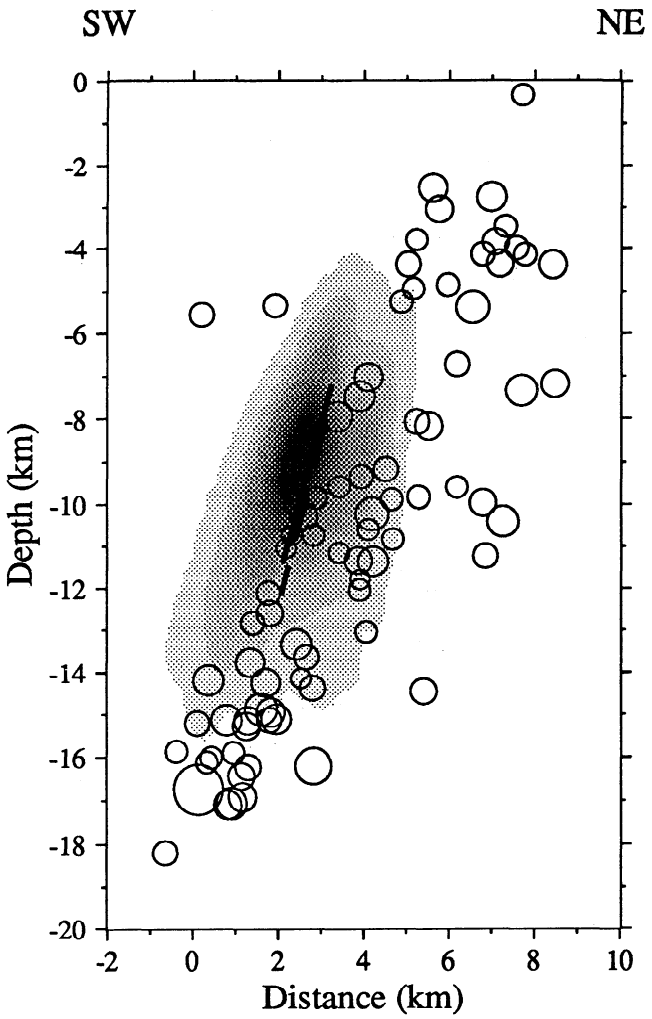

Figure 6. Cross section along azimuth N41°E through the main shock epicenter. The shaded region shows the location of bootstrap models within the 95% confidence limits of the fault parameters. The solid line is the mean of the 2000 bootstrap models, and the dashed line is the best fit model from all the data. The location of the main shock and aftershocks with $M \geq 3.0$ recorded from October 18 to October 31, 1989, are shown with circles. The size of the circles reflect the magnitudes of the earthquakes.

small. This causes the system of equations (6) to be underdetermined, since the number of model parameters ($m = 330$) is greater than the number of data ($n = 326$) and the solution is therefore not unique. To regularize the problem, we add constraints to equation (6) [e.g., *Du et al.*, 1992] and seek an estimate of the slip s that minimizes the function

$$||\mathbf{d} - \hat{\mathbf{d}}(\mathbf{s})||^2 + \beta^2||\nabla^2\mathbf{s}||^2 \quad \text{subject to} \quad s_i \geq 0\,, \quad (7)$$

where the first term is the weighted residual sum of squares (RSS) and the second term is a measure of the "roughness" of the solution; $\nabla^2\mathbf{s}$ is a finite difference approximation to the Laplacian of s [*Harris and Segall*, 1987]. The slip is constrained to be positive, so that only solutions with right-lateral strike slip and reverse dip slip are allowed. This is a reasonable constraint since we do not expect the slip to reverse direction during the earthquake. Without the nonnegativity constraint the solutions can be unstable, with areas of high positive slip alternating with areas of negative slip. The "smoothing" parameter β^2 controls the relative importance of minimizing the residual sum of squares versus minimizing the roughness of the slip. We solve equation (7) by the nonnegative least squares algorithm of *Lawson and Hanson* [1974].

The choice of the smoothing parameter β^2 is a basic problem in inverse theory. Traditionally, β^2 is selected from a "trade-off" curve which plots the trade-off between the fit to the data and some measure of the model complexity. This approach is highly subjective since the choice of β^2 from a trade-off curve is somewhat arbitrary, and the final solution is sensitive to the choice of the smoothing parameter [e.g., *Matthews and Segall*, 1993]. A more rigorous method for estimating smoothing parameters is cross validation [e.g., *Wahba*, 1990; *Matthews and Segall*, 1993]. Here, we use the synthetic data set discussed previously to examine both strategies. We use the results to guide us in choosing the smoothing parameter for the actual Loma Prieta geodetic data.

The philosophy behind cross validation is that one can use $n - 1$ data to generate a model estimate and use that model to predict the omitted datum. A "good" model should predict the omitted data reasonably well. The cross-validation residual is defined as the difference between the omitted datum and the model prediction for that datum. By repeating the calculation for each datum and summing the squared cross-validation residuals we find the cross-validation sum of squares (CVSS). The optimal smoothing parameter is then selected as the value of β^2 that minimizes the CVSS. For nonlinear inversions (with nonnegative least squares) this procedure is computationally intensive and has to be repeated for each value of β^2. Without nonnegativity the problem is linear, and an efficient method of computing the CVSS is available [e.g., *Wahba*, 1990; *Matthews and Segall*, 1993]. We found that leaving out 10% of the data rather than one datum at a time gave similar results and decreased the amount of computation significantly.

In the simulations we can compare the choice of smoothing parameters determined by cross validation and that chosen visually from a trade-off curve with the optimal value of β^2. The optimal value is defined as the value that minimizes $||s - s_{\text{syn}}||^2$, where s_{syn} is the slip distribution used to generate the data. The minimum of $||s - s_{\text{syn}}||^2$ gives the best estimate one could obtain with nonnegative least squares and the chosen smoothing norm.

Simulations

The synthetic data, described in the previous section, are inverted to obtain the predicted slip distribution for a range of smoothing parameters. To examine the resolution of the different data sets, we first treat the

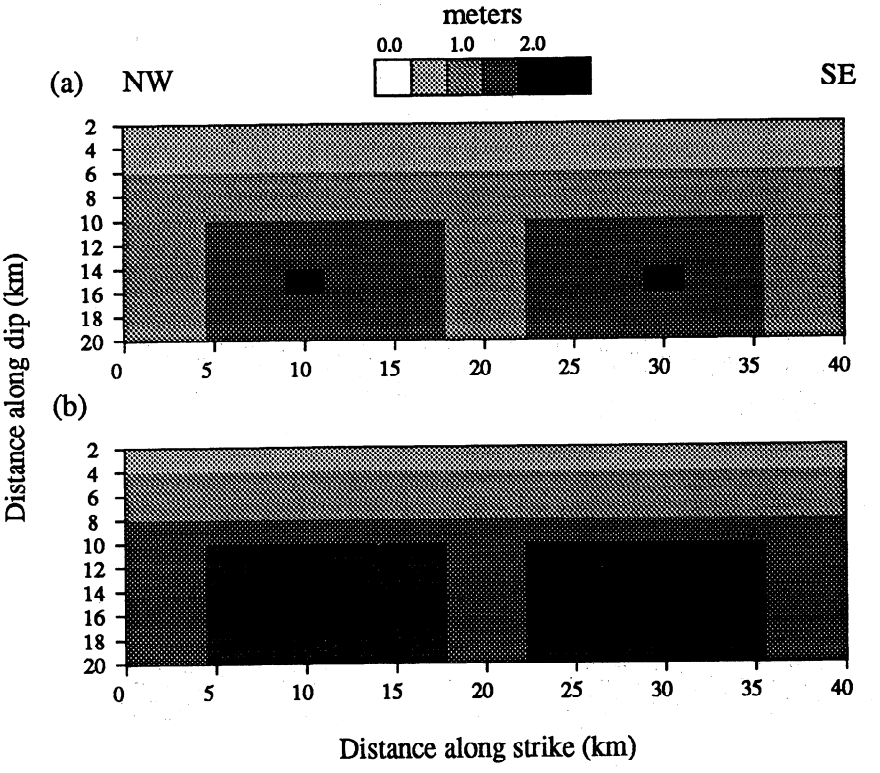

Figure 7. Distributed-slip model used to generate synthetic data. The horizontal coordinate is the distance along strike of the fault from northwest to southeast in kilometers. The vertical coordinate is distance along dip in kilometers. The gray scale bar shows the slip amplitude in meters: (a) strike slip and dip slip (equal), (b) total slip. Right-lateral strike slip and reverse dip slip are both positive. The rake is uniform along the fault at 135° since the magnitudes of the strike-slip and dip-slip components are everywhere equal. The geodetic moment for this model is $M_0 = 2.6 \times 10^{19}$ N m.

leveling data and the combined EDM, GPS, and VLBI data sets separately, and then we combine all the data.

Figures 9a and 9b show the CVSS and $||s - s_{syn}||^2$ as a function of the smoothing parameter, respectively. Both curves exhibit broad minima at smoothing parameters from 5 to 10. Figure 9c shows the trade-off between the fit to the data (RSS) and the model roughness. Based on the trade-off curve, one might choose a somewhat larger value for the smoothing parameter, in the range $\beta^2 = 10 - 25$. Table 2 summarizes the smoothing parameters that minimize the CVSS (β^2_{CVSS}), $||s - s_{syn}||^2$ (β^2_{model}), or qualitatively

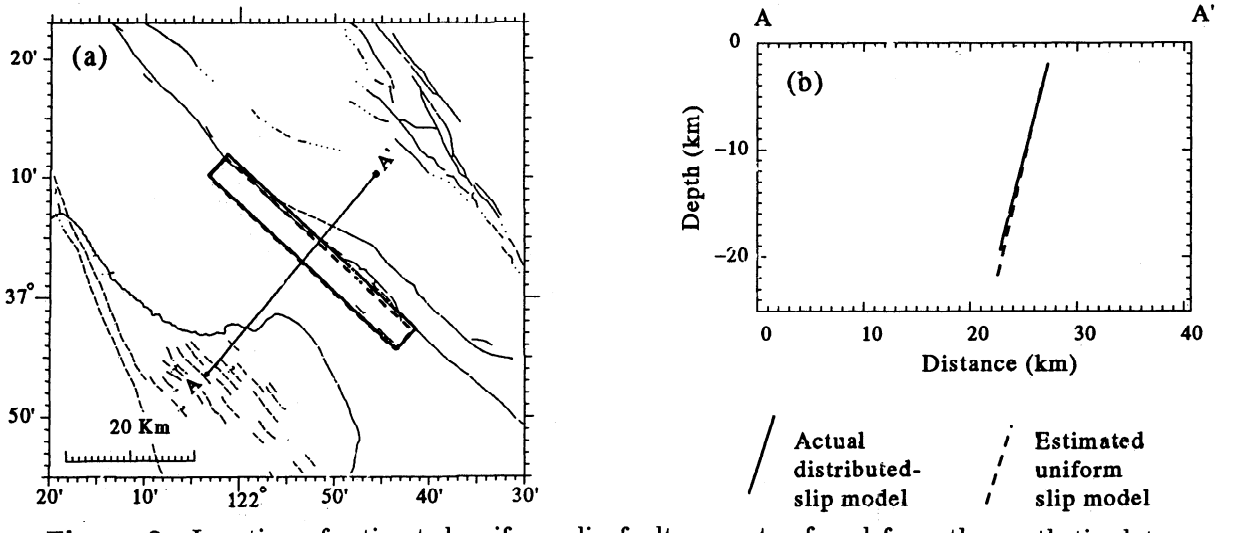

Figure 8. Location of estimated uniform slip fault geometry found from the synthetic data (dashed line) relative to the location of the actual fault model with distributed slip (solid line): (a) map view, and (b) cross section AA′.

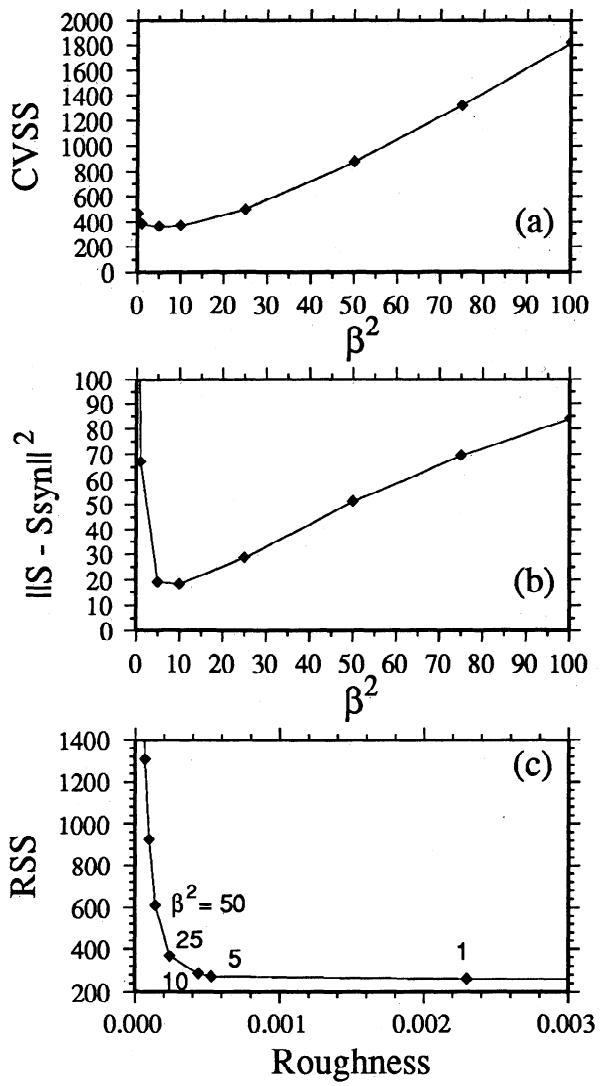

Figure 9. Values of the smoothing parameter for the synthetic data using all the data, minimizing: (a) cross validation, (b) $||s-s_{syn}||^2$, and (c) trade-off between the fit to the data (RSS) and the roughness of the model.

optimize the trade-off between fit to the data (RSS) and roughness of the solution (β^2_{trade}). In summary, cross validation gave an estimate that is essentially optimal, while the trade-off curve yielded a slightly smoother solution.

Figure 10 shows the slip distribution using $\beta^2 = 5$ for the the combined data. Comparing Figures 7 and 10, we see that the estimated slip resolves the bimodal pattern of slip, although the maximum strike slip patch in the northwest part of the fault is not as well resolved.

In the previous section we used the synthetic data from this model and estimated the fault geometry assuming that the slip was uniform. To test for potential bias in the slip estimates, we also use the geometry estimated by the nonlinear optimization, rather than the correct geometry, and solve for the slip distribution. We find that the slip distribution is not significantly different from that obtained with the correct geometry. We conclude that in the case of the Loma Prieta geodetic data, estimating the fault geometry assuming uniform slip and then using that geometry to find the spatially variable slip distribution gives reasonable results. There will be some correlation between the geometry and slip, but in this case they do not appear to be significant.

Distributed-Slip Results

We now present distributed-slip models for the Loma Prieta rupture. We find the optimal smoothing parameter using cross validation for the EDM, GPS, and VLBI data alone, for the leveling data alone, and for the combined data. Figure 11a shows the CVSS as a function of the smoothing parameter for the combined data. The minimum is at $\beta^2 = 1$. For comparison, Figure 11b shows the trade-off curve between the fit to the data (RSS) and the roughness of the model. Smoothing parameters between 2.5 and 5 give models that fit the data well without increasing the roughness of the model significantly. The smoothing parameters that minimize the CVSS for the different data are given in the first column of Table 3. The value of β^2 ranges from 0.5 to 1.0.

The predicted model using all the data and $\beta^2 = 1$ is shown in Figure 12. The slip distribution is very heterogeneous. The pattern of strike slip has several isolated maxima; the most prominent one is in the northwestern part of the fault with up to 5 m of slip at 10 to 14 km depth. There are two small slip patches in the southeastern part of the fault with up to 4 m of slip at 8 to 12 and 6 to 10 km depth. There is a very shallow slip patch in the northwest, extending from the surface to 4 km depth with up to 4 m of slip, which is apparently needed to fit data from stations LP2 and HS5203. These stations are located near the zone of extensive ground ruptures in the Summit Road-Skyland Ridge area (see gray shaded area in Figure 15b [e.g., *Ponti and Wells*, 1991; *U.S. Geological Survey Staff*, 1989]. As a result, data from these stations probably include some inelastic deformation, and it is therefore likely that the shallow slip patches in Figure 12 do not correspond to primary fault slip. The pattern of dip slip shows a single sausage-shaped maximum with up to 8 m of slip at 7 to 11 km depth in the northwest part of the fault. The northwest part of the fault has larger amounts of dip slip than strike slip, whereas the southeast part of the fault has mostly strike-slip motion. The geodetic moment for this model is $M_0 = 3.4 \times 10^{19}$ N m, which is about 17% greater than the moment of the best uniform slip

Table 2. Smoothing Parameter: Synthetic Data from Distributed-Slip Model

Data	β^2_{CVSS}	β^2_{model}	β^2_{trade}
EDM, GPS, and VLBI	5	5	10 - 25
Leveling	5	5	10 - 25
All data	5	10	10 - 25

β^2 is the optimal smoothing parameter. The subscripts denote the different minimization criteria used to obtain β^2. CVSS is the cross-validation sum of squares, model is the difference between the estimated and the synthetic model, $||s - s_{syn}||^2$, and trade is chosen from the trade-off curve between the residual sum of squares and the model roughness.

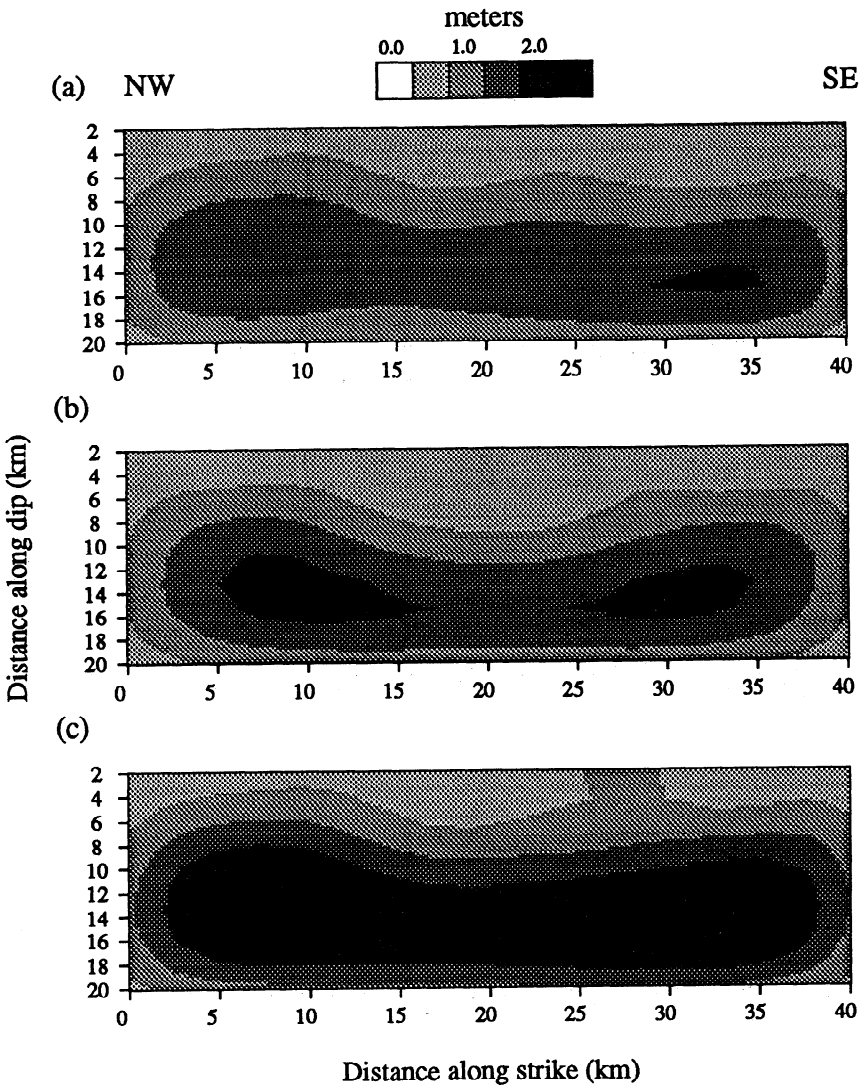

Figure 10. Predicted model from inversion of synthetic data using all the data and a smoothing parameter of $\beta^2 = 5$. The gray scale bar shows the slip amplitude in meters: (a) strike slip, (b) dip slip, and (c) total slip.

model. The moment is within the range estimated from seismic studies (2.3-3.5 $\times 10^{19}$ N m). A larger value of the smoothing parameter ($\beta^2 = 5$), as suggested by the trade-off curve, gives a smoother model with larger areas of slip and smaller slip amplitudes, but the total moment is similar. The main features in the slip pattern are the same, with maximum strike slip and dip slip in the northeastern part of the fault and very little dip slip south of the main shock. We conclude that these features are robust.

Figure 13 shows the slip direction for the preferred model. The size of each arrow is proportional to the slip amplitude. There is a large variation in rake from the southeast part of the fault, where the slip is almost purely right-lateral, to the central part of the fault, where the slip is primarily dip slip, becoming oblique northwest of the main shock. This pattern of slip direction is quite similar to that observed by *Beroza* [1991]. Averaging the rake over the fault plane gives 140°, whereas the rake of the best uniform slip model was 139°. Both are in good agreement with the average rake of 133°± 8° estimated from teleseismic data [*Wallace et al.*, 1991]. Possible mechanisms for the change in rake are discussed below.

Figure 14 shows the observed horizontal displacements with 95% error ellipses determined from the EDM, GPS, and VLBI data and the station displacements predicted by the preferred distributed-slip model. Where there appears only to be one vector, the predicted and the observed displacements are indistinguishable. We see from Figure 14 that the model provides a good overall fit to the data. The largest differences between the observed and predicted data are 6.6 cm at EDM station BIEL and 5.8 cm at EDM station SARGENT. Figure 15a shows the vertical displacements predicted by the preferred slip distribution model, in cm. Figure 15b shows interpolated contours of the weighted vertical residual. The triangles mark the location of the two bench marks (GU2173 and HS5224) that have the highest residual (about 9σ). In general,

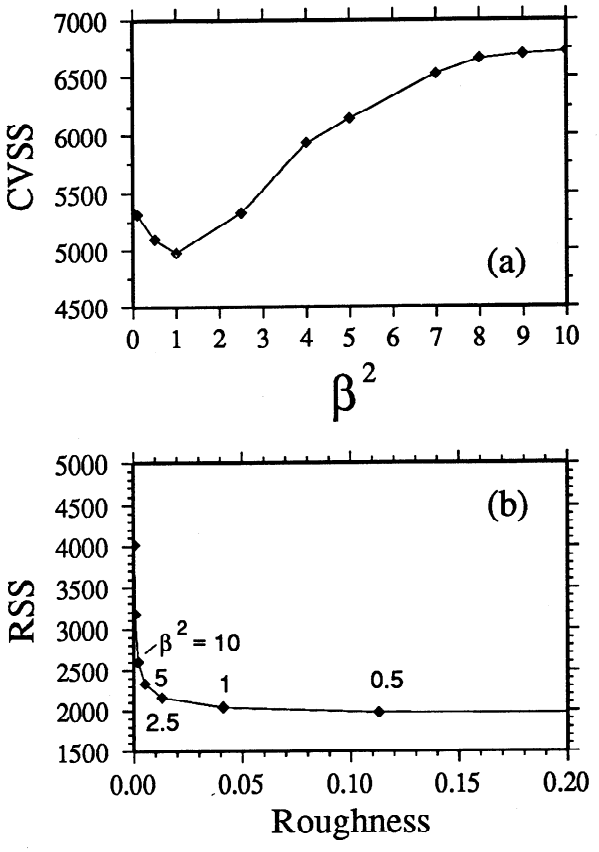

Figure 11. Values of the smoothing parameter for the Loma Prieta geodetic data combining all the data, minimizing (a) cross-validation sum of squares (CVSS) and (b) trade-off between the residual sum of squares (RSS) and the roughness of the model.

the fit to the data is fairly good, and the model captures 91% of the total signal. The areas around Loma Prieta peak and the southern end of the Sargent fault have large residuals in both horizontal and vertical components of the displacement. This indicates that there may be additional sources of deformation that are not included in our model, such as motion on the Sargent fault. *Lisowski et al.* [1994] cite evidence for 2 mm/yr of shallow creep on the southern part of the Sargent fault.

Model Resolution

We examine the model resolution by calculating the surface displacements caused by 1 m of strike slip and 1 m of dip slip on a single fault element and then inverting the synthetic data setting $\beta^2 = 1$. We use the same network of stations and data covariance as in the calculations for the Loma Prieta data. Owing to space limitations we show only the resolution for the total slip here. Figure 16 shows the location of the nine elements that we used in the model resolution calculation (white boxes) and the predicted total slip (gray scale). The resolution was calculated for each element separately, and then the results for three elements were combined in one figure. The maximum slip amplitude is much smaller than the correct slip amplitude; however, the total moment is comparable to the correct moment. In general, we observe that the resolution decreases with increasing depth on the fault. Slip on the northernmost part of the fault is not as well resolved as slip on the central and southern part of the fault. The inferred slip pattern is elongated vertically at shallow depth, almost circular at mid-depth and horizontally elongated at the bottom of the fault. The location of maximum slip is biased toward the surface for the shallow elements (at 2 to 4 km depth), but correlates well with the location of the element that actually slipped at greater depths. This bias at shallow depth is, in part, due to the lack of stations close to the fault trace.

Discussion

We calculated the change in traction acting on the Loma Prieta rupture plane induced by our inferred slip distribution. The maximum local stress drop, which occurs in the area of maximum slip northwest of the hypocenter, is 50 MPa. There are stress increases of up to 10 MPa in the regions surrounding the slip patches. According to our calculations there are regions within the rupture zone in which the stress (particularly the strike-slip component of traction) increased after the earthquake. Given that our ability to resolve slip is limited (Figure 16) and the stress change is proportional to the spatial derivative of slip, we must view the stress change calculations with some caution. For example, it is possible that local stress drops exceed 50 MPa but that we lack the resolution to detect features on that scale.

Figure 17 shows the estimated total slip amplitude relative to the locations of aftershocks with magnitude greater than 1.0 recorded during the last 2 weeks of October 1989. There is some correlation between areas of high slip and an absence of aftershocks; however, one must consider this comparison in light of our ability to resolve spatial variations in slip. The correlation we observe in Figure 17 is perhaps not as strong as that found by *Beroza* [1991]. It is likely that the correlation

Table 3. Cross Validation: Loma Prieta Geodetic Data

Data	β^2	CVSS	M_0, $\times 10^{19}$ N m	RSS	Roughness, $\times 10^{-8}$ km^{-2}
EDM, GPS, and VLBI	0.5	3189	3.6	309	3.9
Leveling	0.5	1658	8.3	808	16.9
All data	1.0	4979	3.4	2041	4.1

β^2 is the optimal smoothing parameter found from cross validation, CVSS is the minimum value of cross-validation sum of squares for the optimal smoothing parameter, RSS is residual sum of squares for that value of the smoothing parameter, M_0 is the geodetic moment, and roughness is the model roughness calculated from the finite difference approximation of the Laplacian.

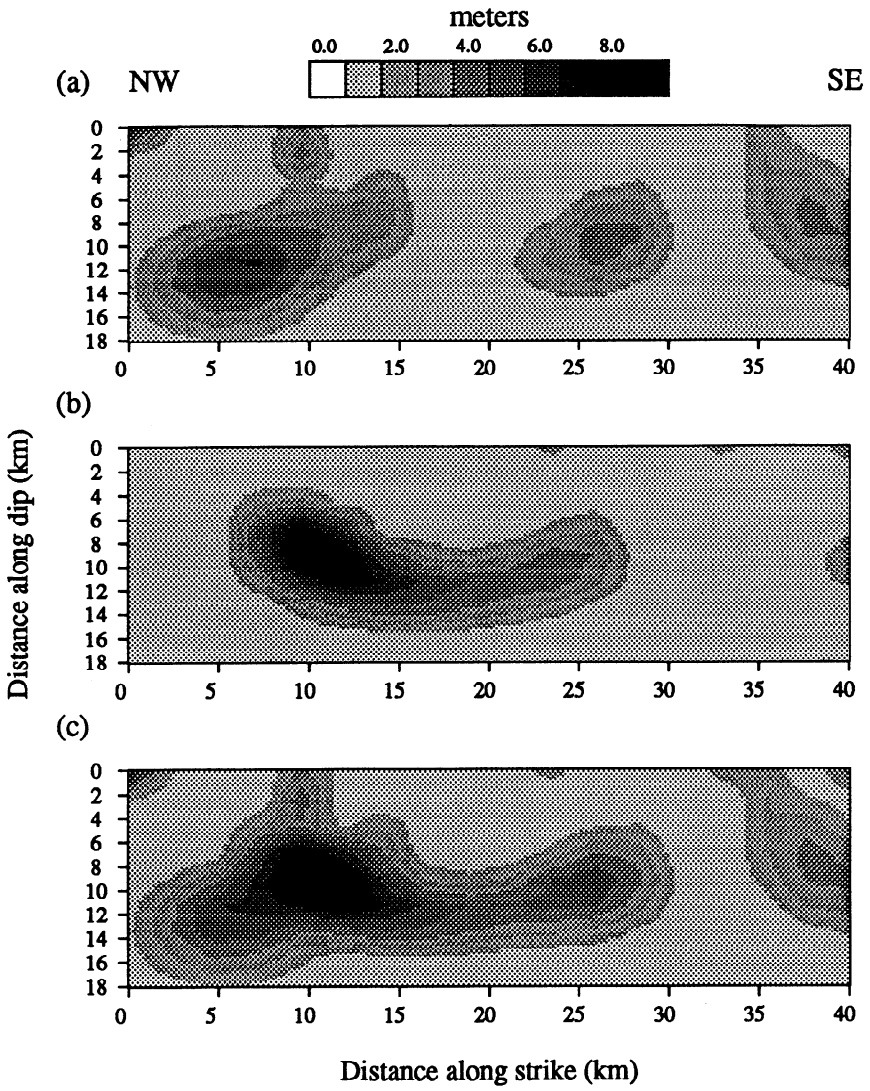

Figure 12. Predicted slip distribution model using all the Loma Prieta geodetic data and a smoothing parameter of $\beta^2 = 1$. The gray scale bar shows the slip amplitude in meters: (a) strike slip, (b) dip slip, and (c) total slip.

between aftershocks and high slip areas could be improved without violating the geodetic observations significantly. The main difference between the preferred model obtained from the geodetic data (Figure 12) and the models of *Beroza* [1991] and *Steidl et al.* [1991] is that the geodetic result has maximum dip slip and maximum strike slip in the northwest part of the fault, whereas their models have maximum strike slip in the southeast and maximum dip slip in the northwest. The geodetic result thus agrees better with the model of *Wald et al.* [1991] in terms of the location of the maximum slip amplitude on the fault. However, our model has no dip slip in the southeast part of the fault, causing the slip direction to vary greatly along strike.

The preferred model, based on a smoothing parameter chosen by cross validation, is significantly more variable in amplitude than comparable models derived from seismic data. Estimated slip amplitude varies from zero

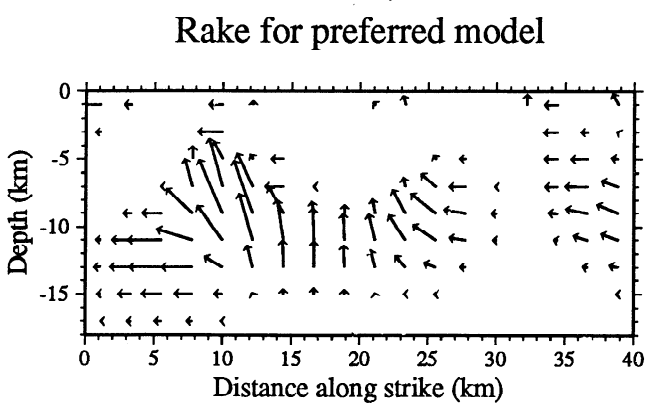

Figure 13. Predicted slip direction for the preferred model using all the Loma Prieta geodetic data and $\beta^2 = 1$. The slip changes direction along the strike of the fault, rotating from almost pure right-lateral strike slip in the southeastern part of the fault, to mostly dip slip and oblique slip in the northwest part. The open areas have no slip.

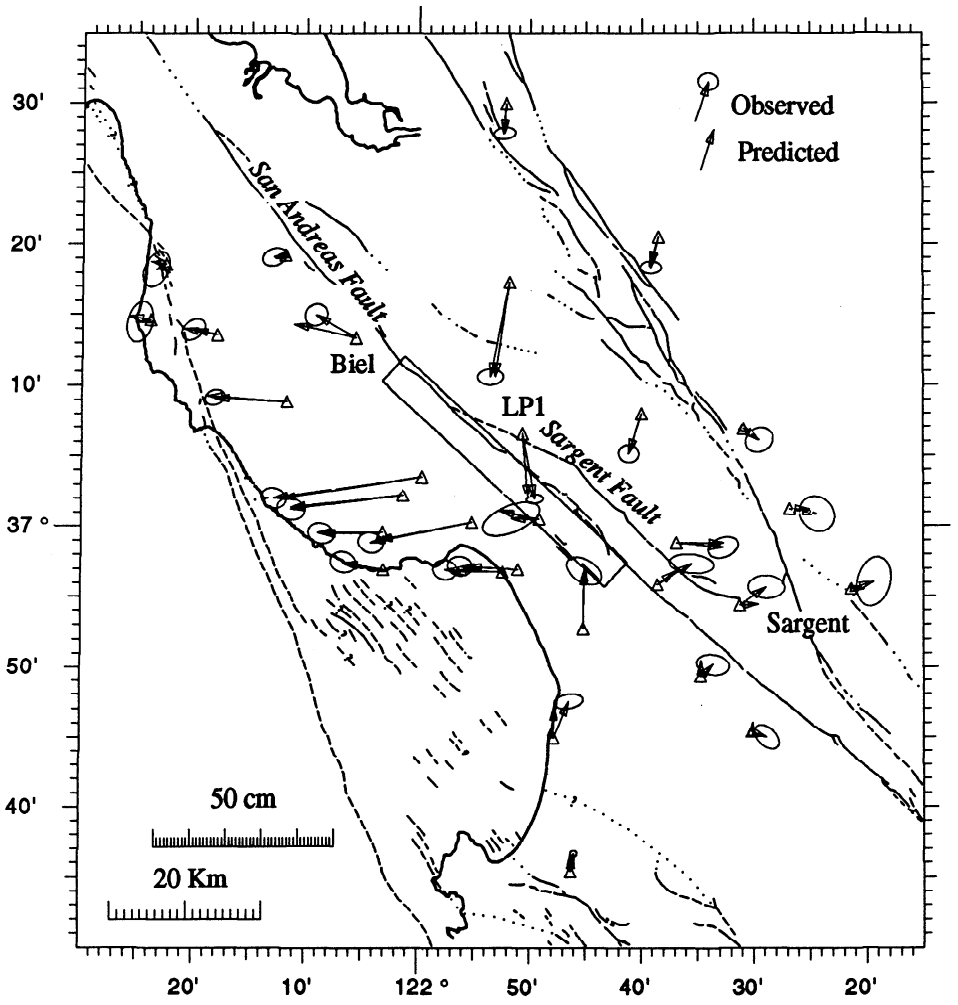

Figure 14. Observed horizontal displacements (vectors with 95% error ellipses) and predicted displacements from the preferred distributed-slip model (Figure 12). The surface projection of the fault model is indicated by a rectangle.

up to 5 m of strike slip and 8 m of dip slip. In contrast, in most of the slip models derived from seismic data the peak slip amplitude is less than 4 m, although *Beroza* [1991] finds up to 5.9 m of slip locally. As noted previously, the variability in the estimated slip depends critically on the choice of smoothing parameter. Our results suggest that previous slip estimates are, to some degree, over damped. Based on our simulations, we believe that the cross-validation estimates of smoothing parameter are reasonable. However, if there are correlations in the data that are not accounted for in our variance-covariance matrices, then cross validation will tend to choose a smoothing parameter that is biased toward nonsmooth distributions. This is because cross validation is based on the premise that signal is spatially correlated while error is not. An example of a correlation that has not been accounted for in our analysis is bench mark instability, which causes opposite signed tilts in the two level sections from that bench mark. We do find similar smoothing parameters from the various independent data sets, which does suggest that cross validation is not being biased by data correlations. If this is so, it implies that the slip distribution in the earthquake is more variable than previously assumed.

Rake Variation

We observe significant variation in rake in the preferred distributed-slip model. In the method used here, the smoothness condition in equation (7) is applied to the strike-slip and dip-slip components separately. Thus we have not directly penalized variations in rake. There are, however, two factors which cause us to believe that the rake variation is likely to be real. First, our simulations (Figure 7) which start with uniform rake produce estimates with nearly uniform rake. Thus there is nothing in the data distribution or the method that biases the result toward variable rake. Second, at least some inversions of the strong motion data exhibit a similar rake variation. It seems unlikely that the different data sets and methodologies used would all be biased in the same sense.

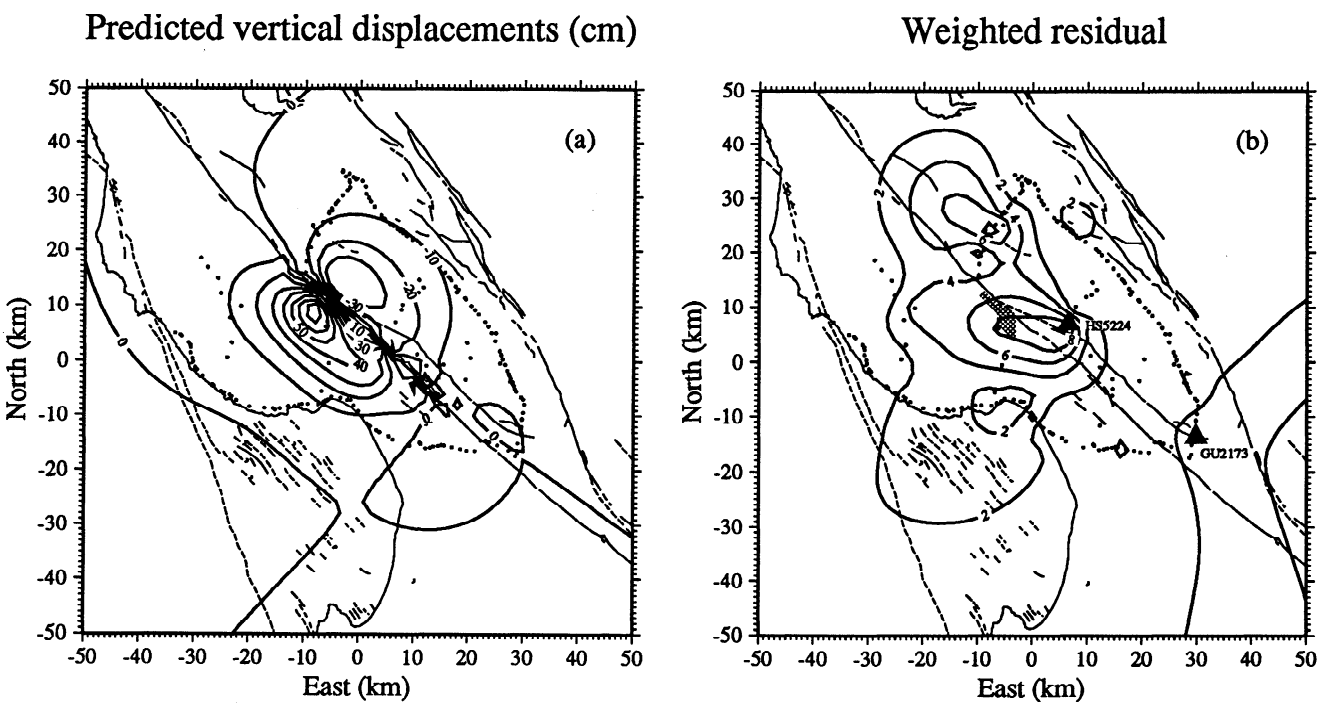

Figure 15. (a) Predicted vertical displacements from the best distributed-slip model, in centimeters. (b) Weighted residual of the vertical displacements and the best distributed-slip model for the combined data. The weighted residual has units of σ. The location of the bench marks are shown with dots. The solid triangles show the location of the two stations that have the largest residuals about 9σ. The shaded region indicates the area of extensive ground cracking and land sliding observed after the 1989 Loma Prieta earthquake [from *U.S. Geological Survey Staff*, 1989].

A common assumption in fault mechanics is that slip occurs in the direction of the maximum resolved shear stress on the fault. If the direction of maximum shear stress changes as a function of position, the rake should change accordingly. It is also commonly assumed that stress is homogeneous within some volume. The fact that we find a nonuniform rake along the Loma Prieta rupture zone appears to require some heterogeneity in stress. While the stress may, in fact, be quite heterogeneous, we show here that the observed change in rake can be explained by a small change in fault dip.

For the sake of discussion, we divide the fault into two parts where the direction of slip changes. The average rake for the northwest part of the fault (from 0 km to 28 km along the strike of the fault model) is 135°. The rake is 165° for the southeastern part of the fault (from 28 km to 40 km along strike). Given that the San Andreas fault is a dominantly strike-slip environment, we assume that the maximum and minimum principal stresses are horizontal and the intermediate stress is vertical. Following *Segall and Lisowski* [1990], we calculate the horizontal and vertical shear stresses τ_h and τ_v from

$$\tau_h = (\sigma_3 - \sigma_1)\cos\theta\sin\theta\sin\delta\,, \tag{8}$$

and

$$\tau_v = [(\sigma_2 - \sigma_3) - (\sigma_1 - \sigma_3)\sin^2\theta]\cos\delta\sin\delta\,, \tag{9}$$

respectively, where δ is the fault dip, $\sigma_1 \geq \sigma_2 \geq \sigma_3$ are the principal stresses and θ is the angle from the normal to the fault to the direction of σ_3, measured clockwise. We define α as the ratio of strike slip and dip slip on the fault,

$$\tau_h = \alpha\tau_v\,. \tag{10}$$

In the preferred model, $\alpha_1 = 1.0$ for the northwestern part of the fault, and $\alpha_2 = 3.7$ for the southeastern part. Combining equations (8), (9), and (10) gives

$$\Phi = \sin^2\theta - \frac{\cos\theta\sin\theta}{\alpha\cos\delta}\,, \tag{11}$$

where $\Phi = (\sigma_2 - \sigma_3)/(\sigma_1 - \sigma_3)$. The ratio of stress magnitudes, Φ is zero if $\sigma_2 = \sigma_3$ and one if $\sigma_2 = \sigma_1$. Assume, for the moment, that the observed change in rake is due to rotation of the stress about a vertical axis. We can then solve equation (11) for the required rotation, for a given value of Φ. We find that the stress orientation must rotate by at least 14° counterclockwise, assuming Φ is a constant. *Gephart* [1994] finds considerable variation in the postseismic principal stress field orientation from inversion of aftershocks in six subregions of the 1989 Loma Prieta earthquake, indicating that the stress field is heterogeneous on a scale of about 10 km. The variation in the shear stress direction he observes is of the same sense but of much smaller magnitude than the minimum rotation needed to explain the main shock rake change.

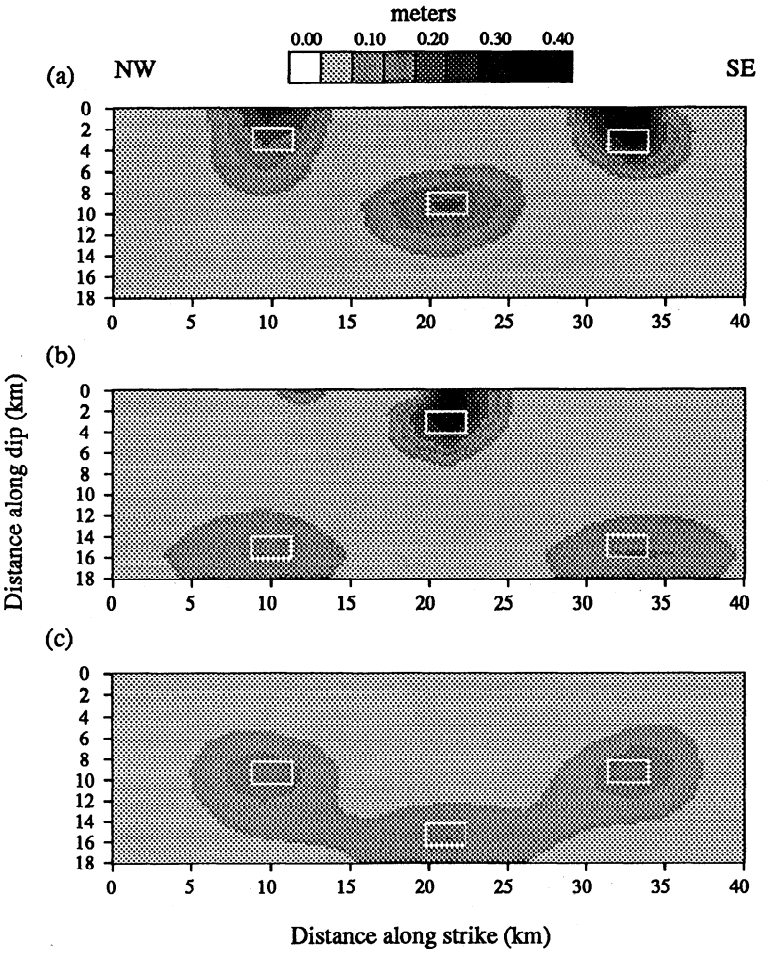

Figure 16. Model resolution for nine elements on the fault. The model resolution is calculated by imposing 1 m of strike slip and 1 m of dip slip on one element and inverting the computed surface deformation using a smoothing parameter of $\beta^2 = 1$. The gray scale shows the total slip in meters from the inversion. The white boxes show the location of the elements used in the model resolution calculation. The predicted slip distribution is calculated for each element and the results for three elements are combined in Figures 16a, 16b, and 16c.

It is also possible that the change in slip direction is due to a change in dip of the fault. Equation (11) can be rearranged to read

$$\alpha \cos\delta = \frac{\cos\theta \sin\theta}{\sin^2\theta - \Phi}. \qquad (12)$$

If we assume a uniform stress tensor, then θ and Φ are constants, so the right-hand side of equation (12) is constant. Thus $\alpha_1 \cos\delta_1 = \alpha_2 \cos\delta_2 = \text{const}$. If we take the dip of the northwestern part of the fault to be $\delta_1 = 76°$, we can solve for the dip on the southeastern part of the fault, $\delta_2 \simeq 86°$. This indicates that a 10° change in dip can explain the change in rake. The change in slip direction in our fault model occurs roughly in the same location as an apparent change in dip of the aftershock zone [e.g., *Dietz and Ellsworth*, 1990; Steven Roecker, personal communication , 1994]. We think that the change in fault dip is a likely explanation for the change in slip direction. However, it is also possible that there is some rotation of the principal stress directions.

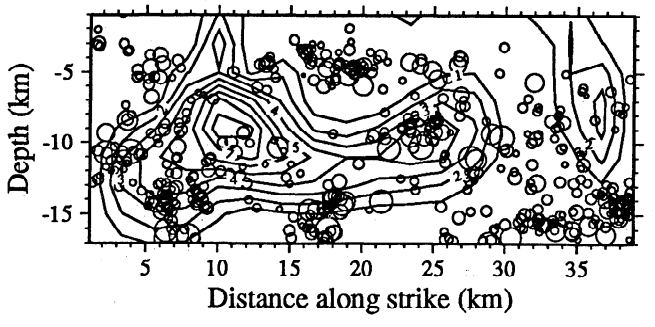

Conclusions

The location and geometry of the Loma Prieta rupture inferred from the inversion of geodetic observations

Figure 17. Predicted slip amplitude for the preferred model using all the Loma Prieta geodetic data and $\beta^2 = 1$. The circles show locations of aftershocks recorded in October 1989. There is little correlation between absence of aftershocks and the area of maximum slip for our model.

are generally consistent with the locations of the aftershocks as well as the main shock focal mechanism. The best fitting rupture surface is located near the southwestern edge of the aftershock zone in the hanging wall of the fault. The fact that the best fitting rupture surface is not within the center of the aftershock zone may be real, due to contrast in elastic properties across the fault, or may be simply due to errors in the data. The set of allowable dislocation models, as determined by bootstrap resampling, overlaps most of the aftershock zone. These results together with numerical simulations demonstrate that high-quality geodetic data combined with quasi-Newton estimation procedures can uniquely determine fault position and geometry. This is important in applying geodetic measurements to the study of interseismic and postseismic deformation where constraints from seismic data are often minimal.

The geodetic data can also be inverted to determine the distribution of slip on the estimated fault surface. Simulations indicate that cross validation is nearly optimal in choosing smoothing parameters for these slip inversions. Using cross validation, we find that the slip distribution on the Loma Prieta rupture surface is very heterogeneous. Slip is concentrated updip and northwest of the hypocenter, where the maximum strike slip is 5 m and the maximum dip slip is 8 m. Our results suggest that other models of fault slip have been over smoothed. The alternative is that there are residual correlations in the data that are not accounted for in our estimates of data covariance and that this biases cross validation toward nonsmooth models.

The estimated slip direction varies considerably over the fault plane. Dominantly right-lateral strike slip occurred southeast of the hypocenter, while the slip northwest of the hypocenter is oblique right-reverse. While this variation in rake could be indicative of spatial variations in stress orientation, it could also be explained by change in fault dip with respect to a uniform regional stress. A change in fault dip of the appropriate sign and magnitude is, in fact, observed in the zone of aftershocks. The fact that the slip direction changes markedly at or near the point where the fault changes dip suggests that changes in the fault geometry played an important role in the rupture dynamics.

Acknowledgments. We are grateful to Mike Lisowski, Grant Marshall, and Ross Stein for access to much of the data used in this study. We thank Ralph Archuleta, Greg Beroza, Dawn Burgess, Yijun Du, Donna Eberhart-Phillips, Bill Ellsworth, Jeff Freymueller, Iain Johnstone, Michael Martin, Jamie Steidl, Larus Thorlacius, Chesley Williams, and David Wald for discussions and comments. Suggestions from Robert King, Jeanne Sauber and an anonymous reviewer helped clarify figures and text. This research was supported by NSF grants EAR-9011226 and EAR-9116117 and the U.S. Geological Survey.

References

Árnadóttir, T., Earthquake dislocation models derived from inversion of geodetic data, Ph.D. thesis, Stanford Univ., Stanford, Calif., 1993.

Árnadóttir, T., P. Segall, and M. Matthews, Resolving the discrepancy between geodetic and seismic fault models for the 1989 Loma Prieta, California, earthquake, *Bull. Seismol. Soc. Am., 82*, 2248–2255, 1992.

Beroza, G. C., Near-source modeling of the Loma Prieta earthquake: Evidence for heterogeneous slip and implications for earthquake hazard, *Bull. Seismol. Soc. Am., 81*, 1603–1621, 1991.

Clark, T. A., C. Ma, J. M. Sauber, J. W. Ryan, D. Gordon, D. B. Shaffer, D.S. Caprette, and N.R. Vandenberg, Geodetic measurement of deformation in the Loma Prieta, California earthquake with very long baseline interferometry, *Geophys. Res. Lett., 17*, 1215–1218, 1990.

Dietz, L. D., and W. L. Ellsworth, The October 17, 1989, Loma Prieta, California, earthquake and its aftershocks: Geometry of the sequence from high-resolution locations, *Geophys. Res. Lett., 17*, 1417–1420, 1990.

Draper, N. R., and H. Smith, *Applied Regression Analysis*, 2nd ed., 709 pp., John Wiley, New York, 1981.

Du, Y., A. Aydin, and P. Segall, Comparison of various inversion techniques as applied to the determination of a geophysical deformation model for the 1983 Borah Peak earthquake, *Bull. Seismol. Soc. Am., 82*, 1840–1866, 1992.

Du, Y., P. Segall, and H. Gao, Dislocations in inhomogeneous media via a modulii perturbation approach: General formulation and two-dimensional solutions, *J. Geophys. Res., 99*, 13,767–13,772, 1994.

Eberhart-Phillips, D., and W. D. Stuart, Material heterogeneity simplifies the picture: Loma Prieta, *Bull. Seismol. Soc. Am., 82*, 1964–1968, 1992.

Efron, B., and R. Tibshirani, Bootstrap methods for standard errors, confidence intervals, and other measures of statistical accuracy, *Stat. Sci., 1*, 54–77, 1986.

Gephart, J. W., Spatial variations in stress from the first six weeks of aftershocks of the Loma Prieta earthquake, in The Loma Prieta, California Earthquake of October 17, 1989, Chapter D, Postseismic Effects, Aftershocks and Other Phenomena, edited by P. Reasenberg, *U.S. Geol. Surv. Prof. Pap. 1550*, in press, 1994.

Gill, P. E. , W. Murray, M. A. Saunders, and M. H. Wright, *Practical Optimization*, 401 pp., Academic, San Diego, Calif., 1981.

Gill, P. E., W. Murray, M. A. Saunders, and M. H. Wright, Users guide for NPSOL: A FORTRAN package for nonlinear programming, *Tech. Rep. SOL 86-2*, Syst. Optim. Lab., Dep. of Operations Res., Stanford Univ., Stanford, Calif., 1986.

Hall, P., and M. Martin, On bootstrap resampling and iteration, *Biometrika, 75*, 661–671, 1988.

Hanks, T. C., and H. Krawinkler, The 1989 Loma Prieta, California, earthquake and its effects: Introduction to the special issue, *Bull. Seismol. Soc. Am., 81*, 1415–1423, 1991.

Harris, R. A., and P. Segall, Detection of a locked zone at depth on the Parkfield, California, segment of the San Andreas fault, *J. Geophys. Res., 92*, 7945–7962, 1987.

Hartzell, S. H., G. S. Stewart, and C. Mendoza, Comparison of L_1 and L_2 norms in a teleseismic waveform inversion for the slip history of the Loma Prieta, California earthquake, *Bull. Seismol. Soc. Am., 81*, 1518–1539, 1991.

Horton, S., J. G. Anderson, and A. Mendez, Frequency domain inversion for the character of rupture during the 1989 Loma Prieta, California earthquake using strong motion and geodetic observations, in The Loma Prieta, California Earthquake of October 17, 1989, Chapter A, Main shock Characteristics, edited by P. Spudich, *U.S. Geol. Surv. Prof. Pap. 1550*, in press, 1994.

Lawson, C. L., and R. J. Hanson. *Solving Least Squares Problems*, Prentice-Hall, Englewood Cliffs, N. J., 1974.

Lisowski, M., W. H. Prescott, J. C. Savage, and M. J. Johnston, Geodetic estimate of coseismic slip during the 1989 Loma Prieta, California, earthquake, *Geophys. Res. Lett., 17*, 1437–1440, 1990.

Lisowski, M., M. H. Murray, and J. L. Svarc, Geodetic measurements of coseismic horizontal deformation, in The Loma Prieta, California Earthquake of October 17, 1989, Chapter A, Main shock Characteristics, edited by P. Spudich, *U.S. Geol. Surv. Prof. Pap. 1550*, in press, 1994.

Marshall, G. A., and R. S. Stein, Elevation changes associated with the October 17, 1989, Loma Prieta earthquake and their use to infer fault slip geometry, in The Loma Prieta, California Earthquake of October 17, 1989, Chapter A, Main shock Characteristics, edited by P. Spudich, *U.S. Geol. Surv. Prof. Pap. 1550*, in press, 1994.

Marshall, G. A., R. S. Stein, and W. Thatcher, Faulting geometry and slip from co-seismic elevation changes: The 18 October 1989, Loma Prieta, California, earthquake, *Bull. Seismol. Soc. Am., 81*, 1660–1693, 1991.

Matthews, M. V., and P. Segall, Statistical inversion of crustal deformation data and estimation of the depth distribution of slip in the 1906 earthquake, *J. Geophys. Res., 98*, 12,153–12,163, 1993.

McNally, K., and S. N. Ward, The Loma Prieta earthquake of October 17, 1989: Introduction to the special issue, *Geophys. Res. Lett., 17*, 1177, 1990.

Okada, Y., Surface deformation due to shear and tensile faults in a half-space, *Bull. Seismol. Soc. Am., 75*, 1135–1154, 1985.

Ponti, D. J., and R. E. Wells, Off-fault ground ruptures in the Santa Cruz Mountains, California: Ridge-top spreading versus tectonic extension during the 1989 Loma Prieta earthquake, *Bull. Seismol. Soc. Am., 81*, 1480–1510, 1991.

Savage, J.C., M. Lisowski, and J.L. Svarc, Postseismic deformation following the 1989 (M=7.1) Loma Prieta, California, Earthquake, *J. Geophys. Res., 99*, 13,757–13,765, 1994.

Segall, P., and M. Lisowski, Surface displacements in the 1906 San Francisco and 1989 Loma Prieta earthquakes, *Science, 250*, 1241–1244, 1990.

Snay, R. A., H. C. Neugebauer, and W. H. Prescott, Horizontal deformation associated with the Loma Prieta earthquake, *Bull. Seismol. Soc. Am., 81*, 1647–1659, 1991.

Steidl, J. H., R. J. Archuleta, and S. H. Hartzell, Rupture history of the 1989 Loma Prieta, California, earthquake, *Bull. Seismol. Soc. Am., 81*, 1573–1602, 1991.

Steidl, J. H., and R. J. Archuleta, The 1989 Loma Prieta, California, earthquake: Are geodetic measurements and rupture models consistent?, in The Loma Prieta, California Earthquake of October 17, 1989, Chapter A, Main shock Characteristics, edited by P. Spudich, *U.S. Geol. Surv. Prof. Pap. 1550*, in press, 1994.

U.S. Geological Survey Staff, Preliminary map of fractures formed in the Summit Road-Skyland Ridge area during the Loma Prieta, California, earthquake of October 17, 1989, scale 1:12000, *U.S. Geol. Surv., Open File Rep., 89–668*, 1989.

Wahba, G., *Spline Models for Observational Data*, Society for Industrial and Applied Mathematics, Philadelphia, Pa., 1990.

Wald, D. J., D. V. Helmberger, and T. H. Heaton, Rupture model of the 1989 Loma Prieta earthquake from the inversion of strong motion and broadband teleseismic data, *Bull. Seismol. Soc. Am., 81*, 1540–1572, 1991.

Wallace, T. C., A. Velasco, J. Zhang, and T. Lay, A broadband seismological investigation of the 1989 Loma Prieta, California, earthquake: Evidence for deep slow slip?, *Bull. Seismol. Soc. Am., 81*, 1622–1646, 1991.

Williams, C., T. Árnadóttir, and P. Segall, Coseismic deformation and dislocation models of the 1989 Loma Prieta earthquake derived from Global Positioning System measurements *J. Geophys. Res., 98*, 4567–4578, 1993.

T. Árnadóttir, Department of Geology, Victoria University, P.O. Box 600, Wellington, New Zealand. (e-mail: thora@gphs.vuw.ac.nz)

P. Segall, Department of Geophysics, Stanford University, Stanford, CA 94305. (e-mail: segall@kilauea.stanford.edu)

(Received November 16, 1993; revised May 11, 1994; accepted May 13, 1994.)